Citation: Kuhn, M., and C. Hirt (2016), Topographic gravitational potential up to second-order derivatives: an examination of approximation errors caused by rock-equivalent topography (RET), *Journal of Geodesy* 90(9), 883-902, doi:10.1007/s00190-016-0917-6.

Topographic gravitational potential up to second-order derivatives: an examination of approximation errors caused by rock-equivalent-topography (RET)

Michael Kuhn (corresponding author)
Western Australian Centre for Geodesy & The Institute for Geoscience Research,
Curtin University, GPO Box U1987, Perth, WA 6845, Australia
Phone: +61-8-92667603, Fax: +61-8-92662703, Email: m.kuhn@curtin.edu.au

Christian Hirt
Institute for Astronomical and Physical and Geodesy & Institute for Advanced Study
Technische Universität München, Germany
Email: c.hirt@tum.de

Abstract

In gravity forward modelling, the concept of Rock-Equivalent-Topography (RET) is often used to simplify the computation of gravity implied by rock, water, ice and other topographic masses. In the RET concept topographic masses are compressed (approximated) into equivalent rock, allowing the use of a single constant mass-density value. Many studies acknowledge the approximate character of the RET, but few have attempted yet to quantify and analyse the approximation errors in detail for various gravity field functionals and heights of computation points. Here we provide an in-depth examination of approximation errors associated with the RET compression for the topographic gravitational potential and its first- and second-order derivatives. Using the Earth2014 layered topography suite we apply Newtonian integration in the spatial domain in the variants (a) rigorous forward modelling of all mass bodies, (b) approximative modelling using RET. The differences among both variants, which reflect the RET approximation error, are formed and studied for an ensemble of 10

different gravity field functionals at three levels of altitude (on and 3 km above the Earth's surface and at 250 km satellite height).

The approximation errors are found to be largest at the Earth's surface over RET compression areas (oceans, ice shields) and to increase for the first- and second-order derivatives. Relative errors, computed here as ratio between the range of differences between both variants relative to the range in signal, are at the level of 0.06-0.08 % for the potential, ~3-7% for the first-order derivatives at the Earth's surface (~0.1 % at satellite altitude). For the second-order derivatives, relative errors are below 1% at satellite altitude, at the 10-20% level at 3 km and reach maximum values as large as ~20 to 110 % near the surface. As such, the RET approximation errors may be acceptable for functionals computed far away from the Earth's surface or studies focussing on the topographic potential only. However, for derivatives of the functionals computed near the Earth's surface, the use of RET introduces very spurious errors, in some cases as large as the signal, rendering it useless for smoothing or reducing of field observation, thus rigorous mass modelling should be used for both spatial and spectral domain methods.

Keywords: Rock-Equivalent Topography (RET); Topographic potential; First and second-order derivatives; Spherical Approximation; Discretized Newtonian integration

1 Introduction

Approximation of the 'real' topography by Rock-Equivalent-Topography (RET) is a common concept used when modelling gravitational effects of the Earth's topography (e.g. Lee and Kaula 1967, Balmino et al. 1973, Rummel et al. 1988, Wieczorek 2015) or when inferring geophysical parameters from relations between Earth's topography and its gravity field (e.g. Lambeck 1976). The RET concept replaces a mass distribution with varying density by a simplified distribution of equal mass and constant mass-density (e.g. RET reference density). While the RET concept can relate to any mass anomaly (e.g. topography, crust, mantle, etc.) it is usually referred to the Earth's topography including oceans, ice sheets and lakes. In this study we use the term RET but acknowledge that there is no consistent terminology and, amongst others, terms like Equivalent Rock Topography (e.g. Lee and Kaula 1967, Balmino et al. 1973), Equivalent Rock Height (e.g. Kuhn and Seitz 2005, Baran et al. 2006), and Rock Equivalent Heights (e.g. Makhloof and Ilk 2008a, Grombein et al. 2010, 2014b) are in use.

Underlining the importance of this study, a large number of studies have and continue to use the RET concept for simplified modelling of gravitational effects induced by the Earth's topography (e.g. Chambat and Valette 2005, Kuhn and Seitz 2005, Kuhn et al. 2009, Grombein et al. 2010, Hirt and Kuhn 2012, Hirt 2013, Claessens and Hirt 2013, Hirt and Kuhn 2014, Hirt et al. 2014, Hirt et al. 2015, Forsberg and Jensen 2015, Hirt et al. 2016) and of isostatic compensation masses (e.g., Sünkel 1985, Rummel et al. 1988, Pavlis and Rapp 1990, Tsoulis 1999, Heck and Wild 2005, Wild and Heck 2005, Makhloof and Ilk 2008a, 2008b, Göttl and Rummel 2009, Bagherbandi 2011, Tsoulis and Patlakis 2013, Grombein et al. 2014a, 2014b). For the construction of synthetic Earth gravity models, the RET concept is frequently used allowing the synthetic model to be based on simplified mass sources (e.g. Haagmans 2000, Kuhn and Featherstone 2003, 2005, Claessens 2003, Baran et al. 2006, Tsoulis and Kuhn 2007, Fellner et al. 2012). Spectral analysis of the Earth's shape and induced gravitational field also benefits from the RET concept (e.g. Lee and Kaula 1967, Balmino et al. 1973, Jekeli 1983, Rapp 1982, 1989, Balmino et al. 2012, Tsoulis and Patlakis 2013, Rexer and Hirt 2015). Most of the studies listed above focus on global gravity field modelling where the RET concept is often used to smooth satellite-based gravity field observations. However, some studies also use the RET concept for regional gravity field modelling on or close to the Earth's surface with focus on (Bouguer) gravity anomalies or the provision of fill-in gravity information (e.g. Hirt 2013, Forsberg and Jensen 2015).

In geophysical applications the RET concept is often deployed to infer parameters of the solid Earth such as density variations (e.g. Arkani-Hamed 1970, Lambeck 1979, Matyska 1989), crustal thickness (e.g. van Hees 2000, Llubes et al. 2003, Zhang 2005, Petrov et al. 2016), elastic thickness of the lithosphere (e.g. Stark et al. 2003, Kirby and Swain 2008, Audet 2014, McKenzie 2010, McKenzie et al. 2015) and mantle convection (e.g. Cadek and Matyska 1990, 1991). In the geophysical literature, the RET concept is also known as *bathymetric correction* used in computations of Bouguer gravity anomalies at sea where ocean water is replaced by an equivalent rock layer (e.g. Sleep and Fujita 1997, Tsoulis 2001, Tziavos and Sideris 2013).

Several studies have acknowledged the advantages and disadvantages of using the RET concept. Most argue that the main advantage is the use of a single constant mass density for all masses, allowing for simplified modelling (e.g. Pavlis and Rapp 1990, Kuhn and Feathersone 2005, Kuhn and Seitz 2005, Tsoulis and Kuhn 2007, Göttl and Rummel 2009, Grombein et al. 2010, Hirt and Kuhn 2012, Hirt 2013, Hirt et al. 2014, Kalberg et al. 2015).

For example, Pavlis and Rapp (1990) note, when modelling gravitational effects, the use of a single constant mass density provides considerable save of computational resources. This is because time-consuming evaluation of Newton's integral in both the space and frequency domains (e.g. Kuhn and Seitz 2005, Hirt and Kuhn 2014) has to be performed only once rather than as often as there are different mass anomalies. Moreover, the use of a constant density allows for joint simplified modelling of both topographic and isostatic compensation masses for spherical harmonic representations of the induced gravitational field (e.g. Rummel et al. 1988, Göttl and Rummel 2009). However, this simplification comes at the expense of a change in mass distribution in both geometry and density of the topographic masses whenever the mass considered has a density different to the RET reference density. This is most notably the case for ocean water and ice (e.g. Tsoulis and Kuhn 2007). In some instances, the approximation may be permitted when dealing with local topographic loads where mass equivalence guarantees equal loads. However, because a change in mass distribution usually results in a change of the induced gravitational field, the RET concept introduces errors in gravity field modelling based on topographic mass models.

Even though approximation errors associated with the RET concept are often acknowledged, their magnitude has rarely been quantified. Grombein et al. (2010) has demonstrated the effect on gravity gradients at GOCE (Gravity Field and Steady-State Ocean Circulation Explorer) flight altitude showing approximation errors to a maximum level of 24 mE ($1E = 10^{-9}s^{-2}$) over deep ocean areas, which is well above the GOCE measuring accuracy of 1-2 mE (for the diagonal components M_{11}, M_{22}, M_{33} and off-diagonal element M_{13}, of the Eötvös tensor, e.g. Rummel at al. 2011) and an adequate level of accuracy of well below 1 mE for modelled gravity gradients effects from topographic masses. Therefore, Grombein et al. (2010) recommend that a rigorous (separate) modelling of all mass distributions should be done in favor of the RET concept. Some other studies now consider the more rigorous approach by separate modelling of all mass distributions involved (e.g. Eshagh 2009a, Tenzer et al. 2010, Balmino et al. 2012, Grombein et al. 2014a).

The main aim of this study is to provide a rigorous and comprehensive quantification of approximation errors associated with the RET-concept based on comparisons with rigorous modelling of rock, ice and water mass bodies. Apart from focusing on common RET applications in satellite gravity field modelling only this study also focuses on less common airborne and terrestrial applications so to provide a comprehensive insight into potential

approximation errors. For this, approximation errors are investigated for commonly used gravitational functionals, the gravitational potential and its first- and second-order derivatives. Furthermore, each gravity functional is modelled at the most common observation or modelling locations, e.g., (i) at the Earth's surface (or close to it; e.g. terrestrial), (ii) at an air plane flight height of 3 km (e.g. air-borne) and (iii) at a satellite flight height of 250 km (e.g. GOCE; space-borne) accounting for the attenuation of gravity with height.

2 Data and Methods

2.1 Topography Data

The topographic masses used in this study are based on the Earth2014 model suite (Hirt and Rexer 2015, http://ddfe.curtin.edu.au/gravitymodels/Earth2014/). Here we use the Earth2014 5 arc-minute topography grids representing the Earth's surface heights H_{SUR} (component "SUR2014" representing the interface between solid or liquid masses and air), bedrock heights H_{BED} (component "BED2014") and thickness of the major ice sheets over Greenland and Antarctica ΔH_{ICE} (component "ICE2014"). From these we derive five major mass bodies describing the Earth's topography (cf. Figure 1) including (1) dry bedrock masses above Mean Sea Level (MSL), (2) ocean water masses, (3) ice sheet masses, (4) major lake water masses (Great Lakes, Caspian Sea and Lake Baikal), and (5) air masses below MSL (e.g. dry bedrock below MSL). As such, in this study, the term 'Earth's topography' refers to the envelope of all five mass bodies described above. Note that the Earth2014 model suite also provides a pre-computed RET-layer in planar approximation, which, however, is not used here (cf. Sect. 2.2).

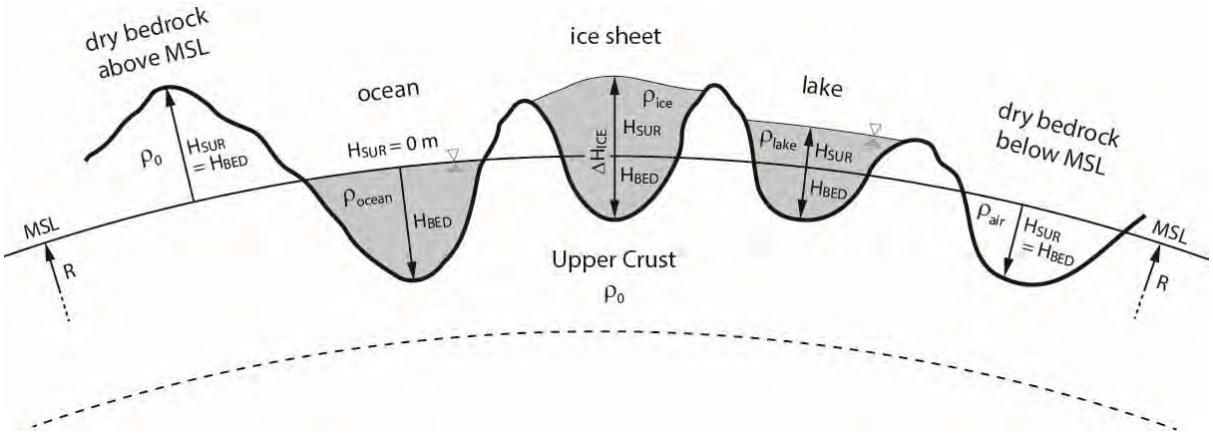

Figure 1: Major terrain types characterizing the Earth topography in spherical approximation. Terrain types are described by their respective heights above (positive)/below (negative) the MSL (e.g. mean sphere with radius R).

The mass bodies are described by their horizontal and vertical extensions and mass-density values. While the horizontal extension is given by the extension of the gridded data (e.g. 5 arc-minute by 5 arc-minute) the vertical extension is described by their respective heights above (positive)/below (negative) MSL. The mass-density values used in this study are summarized in Table 1.

Table 1: Mass-density values used in this study.

Mass Type	Density Value [kg×m^{-3}]
RET	2670
Bedrock	2670
Ocean water	1030
Lake water	1000
Ice	927
Air	approx. 0

2.2 The Rock-Equivalent-Topography Concept

Following the principle of Balmino et al. (1973), Rock-Equivalent Topography (RET) is obtained by 'compressing' all mass anomalies above the bedrock into equivalent rock mass. A general expression for the RET height is given by

$$H_{RET} = H_{BED} + \Delta H_c \tag{1}$$

where H_{BED} is the height of the bedrock and ΔH_c is the (effective) thickness of the mass body after compression into equivalent rock. Note that the formulation is independent of the approximation level used for the height reference surface. Height values used in this notation are measured above (positive)/below (negative) a given reference surface (e.g. MSL). The (effective) thickness ΔH_c can be the result of either a single or multiple mass anomalies 'stacked' onto each other. For clarity here we present the RET concept using a single mass anomaly at a given location which, however can be easily extended to multiple mass anomalies if required (e.g. Claessens 2003, Hirt 2014, Hirt and Rexer 2015). The determination of ΔH_c is based on the principle of local mass equivalence – within the same mass column – between anomalous masses of density ρ and compressed masses using the RET reference density ρ_0. The latter is usually equal to the density of bedrock (e.g., mean density of the Earth's upper crust). Depending on the approximation level used (e.g. planar, spherical, elliptical, etc.) the determination of ΔH_c will vary. In planar approximation the well-known relation

$$\Delta H_c = \frac{\rho}{\rho_0}\Delta H = \frac{\rho}{\rho_0}\left(H_{up} - H_{low}\right) \qquad (2)$$

is used, where the vertical extension (e.g. thickness ΔH) of the anomalous mass is scaled by the ratio ρ/ρ_0 of the respective densities involved (e.g. Balmino et al. 1973). The anomalous masses are characterized by the heights of their respective upper and lower limits, H_{up} and H_{low} where $H_{low} = H_{BED}$ when dealing with a single mass anomaly (cf. Figure 2).

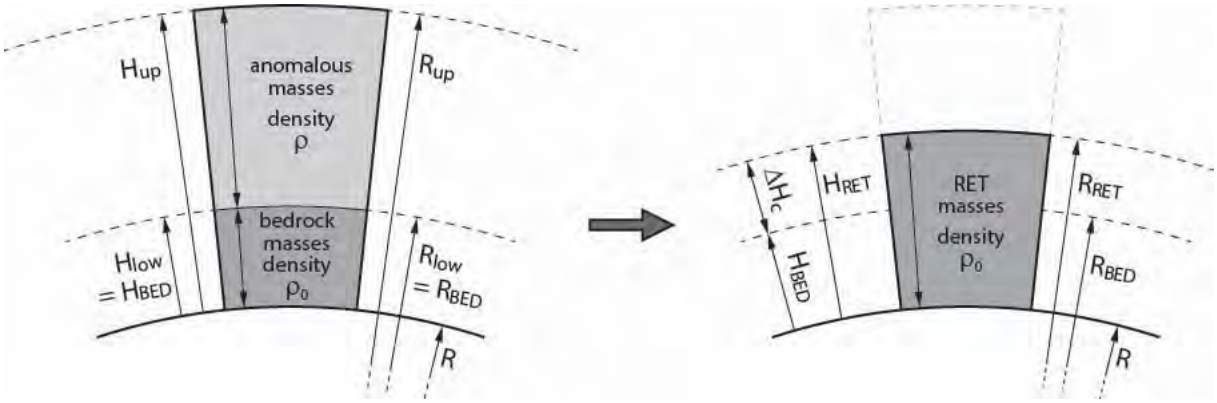

Figure 2: RET principle in spherical approximation for a single mass anomaly. Left: Anomalous masses with density ρ located on top of bedrock masses. The vertical extension of the anomalous masses is given by H_{up} and $H_{low} = H_{BED}$. Right: RET masses with reference density ρ_0 located on the mean sphere with radius R. The vertical extension of the RET masses is given by $H_{RET} = H_{BED} + \Delta H_c$ (cf. eq. 1).

In this study we consistently employ spherical approximation for both the calculation of H_{RET} and gravitational effects (cf. section 2.3). This is different to many previous studies that frequently use planar approximation for the calculation of H_{RET} but employ spherical approximation for the calculation of gravitational effects. Claessens (2003) showed that maximum relative differences between planar and spherical H_{RET} are below 0.1% for a maximum ocean depth of 11 km, thus could be considered to be negligible. However, to ensure consistency with the calculation of gravitational effects we use H_{RET} in spherical approximation. At a given column (e.g. grid element), mass equivalence between the anomalous masses and the RET masses in spherical approximation satisfies the condition (e.g. Rummel et al. 1988, eq. 13)

$$\rho \int_{r=R_{low}}^{r=R_{up}} r^2 dr = \rho_0 \int_{r=R_{low}}^{r=R_{low}+\Delta H_c} r^2 dr \quad \Leftrightarrow \quad \rho\left[R_{up}^3 - R_{low}^3\right] = \rho_0\left[\left(R_{low} + \Delta H_c\right)^3 - R_{low}^3\right] \qquad (3)$$

with the spherical radii $R_{up} = R + H_{up}$ and $R_{low} = R + H_{low}$, representing the upper and lower limits of the mass anomaly, respectively (cf. Figure 2). Based on Eq. (3) the height change of the compressed mass anomaly is given by (e.g. Kuhn and Seitz 2005)

$$\Delta H_c = \sqrt[3]{\frac{\rho}{\rho_0}\left(R_{up}^3 - R_{low}^3\right) + R_{low}^3} - R_{low}. \tag{4}$$

It is important to note that the formalism given in Eqs. (1) to (4) does not require discrimination between mass anomalies above and below MSL. This implicitly ensures mass anomalies above and below MSL are modelled by the respective mass-density values ρ and $\Delta\rho = \rho_0 - \rho$ (see appendix A for numerical proof). This is consistent with the definition of mass anomalies as differences to an idealized Earth's upper crust having the constant density ρ_0 and upper bound of a mean sphere with radius R.

2.3 Forward Gravity Modelling

We employ the principle of *discretized* Newtonian integration (e.g. Kuhn 2000, 2003, Kuhn et al. 2009, Hirt and Kuhn 2014) to derive the gravitational potential and its first- and second-order derivatives induced by the topographic or RET masses. This approach evaluates Newton's integral through numerical integration by dividing (discretizing) the mass distribution into a set of regularly shaped mass elements (e.g. point mass, prisms or tesseroids) whose gravitational field can be computed analytically. The gravitational effect of the complete mass distribution is then obtained through superposition of the individual gravitational effects (e.g., Blakely 1996). For the gravitational potential this principle can be exemplified through the approximation of Newton's integral by (e.g. Hirt and Kuhn 2014)

$$\delta V = G\iiint_M \frac{dm}{l} \approx \sum_{n=1}^{N} G\iiint_{m_n} \frac{dm_n}{l_n} = \sum_{n=1}^{N} \delta V_n \tag{5}$$

where the gravitational potential δV, generated by the complete mass distribution M is obtained by the individual effects δV_n of $n = 1, \ldots, N$ mass elements m_n. In Eq. (5), G is the universal gravitational constant, l and l_n are the Euclidean distances to the running integration points dm and dm_n, which denote infinitesimally small mass elements describing M and m_n, respectively. The sign of δV and δV_n follow that of dm and dm_n, respectively, e.g. positive for mass excess and negative for mass deficiencies. Using the same principle we derive the first-order derivatives of the gravitational potential by

$$\delta\mathbf{g} = \left(\delta g_\varphi, \delta g_\lambda, \delta g_r\right)^T = \nabla(\delta V) \approx \sum_{n=1}^{N} \nabla(\delta V_n) \tag{6}$$

where ∇ denotes the gradient operator and $\delta g_\varphi, \delta g_\lambda, \delta g_r$ are the vector components of gravitational vector $\delta\mathbf{g}$ given here in a local north oriented Cartesian coordinate system with its axis pointing towards north (e.g. increasing spherical latitude φ), towards east (e.g. increasing spherical longitude λ) and upwards (e.g. increasing geocentric radius r). Here, the vector components $\delta g_\varphi, \delta g_\lambda, \delta g_r$ are defined positive for gravitational effects increasing in the opposite directions of the local north oriented Cartesian coordinate system, e.g. positive towards, west, south and downwards. In the same coordinate system, the second-order derivatives of the gravitational potential are obtained by

$$\delta\mathbf{E} = \begin{bmatrix} \delta V_{\varphi\varphi} & \delta V_{\varphi\lambda} & \delta V_{\varphi r} \\ \delta V_{\lambda\varphi} & \delta V_{\lambda\lambda} & \delta V_{\lambda r} \\ \delta V_{r\varphi} & \delta V_{r\lambda} & \delta V_{rr} \end{bmatrix} = \nabla(\nabla\delta V) \approx \sum_{n=1}^{N} \nabla(\nabla\delta V_n) \tag{7}$$

where $\delta\mathbf{E}$ is the symmetric Eötvös tensor containing all gravity gradients (e.g. Moritz and Hofmann-Wellenhof 1993). While $\delta\mathbf{E}$ is also called Marussi tensor (e.g. Hofmann-Wellenhof and Moritz 2005) we follow the notation in Moritz and Hofmann-Wellenhof (1993) which uses the former term to indicate the gradient tensor (e.g. Eq. 7) and the latter to express geometric properties of the gravity field (e.g. Eötvös tensor divided by gravity). The Eötvös tensor contains only five independent components as the diagonal components satisfy the Laplace equation $\delta V_{\varphi\varphi} + \delta V_{\lambda\lambda} + \delta V_{rr} = 0$.

The approximation errors introduced by the mass discretization using Eqs. (5) to (7) depend on how well the individual mass elements approximate the original mass distribution (see section 3.2 for uncertainty estimates). In order to reduce the approximation errors caused by mass elements located in the near vicinity of the computation point we employ the principle of spherical terrain corrections (e.g. Kuhn et al. 2009) where only masses residual to a spherical shell are considered in the discretized Newtonian integration (cf. Figure 3). Exemplified for the gravitational potential this approach is expressed by

$$\delta V = \delta V^{SH} + \delta V^{RM} \tag{8}$$

where δV^{SH} is the gravitational potential of the spherical shell and δV^{RM} is the gravitational potential of all residual masses. Importantly, the vertical dimension of the spherical shell is selected such that no residual masses are present at the location of the computation point. This approach can be applied to any mass distribution (e.g. layer) with irregular top and bottom surfaces (cf. Figure 3).

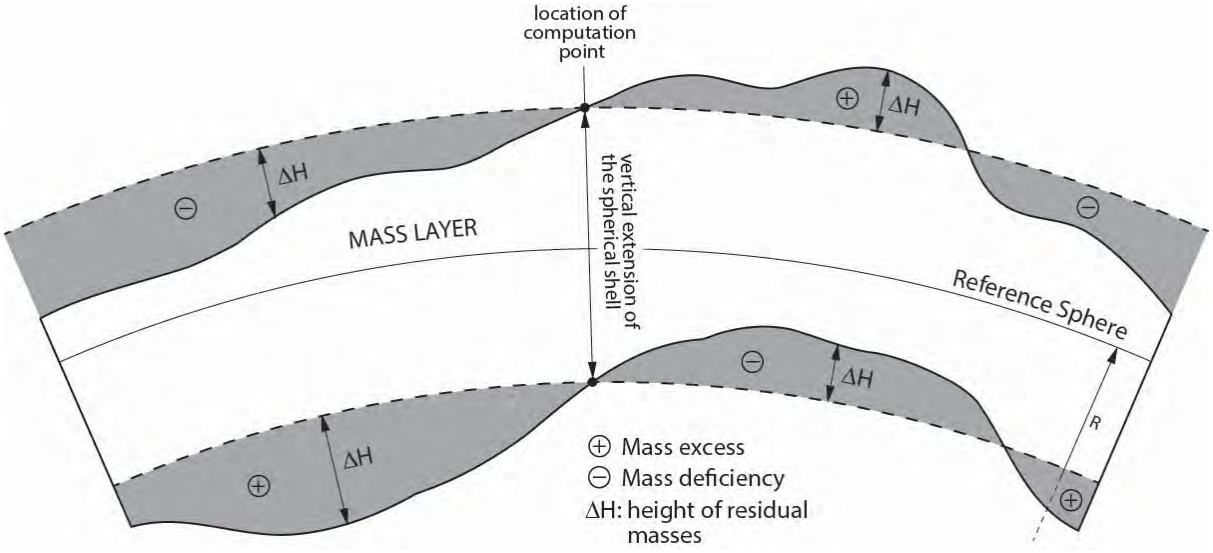

Figure 3: Schematic illustration of the generalized concept of spherical terrain corrections for a mass distribution (layer) with variable top and bottom surface (thick solid line). In this concept only masses that are residual to a spherical shell (dashed lines) are considered. The spherical shell is selected so that no residual masses are present at the location of the computation point P. Residual masses outside and inside the shell act as mass excess and deficiencies, respectively.

For practical evaluation of Eqs. (5) to (7) we use as elementary mass elements spherical volume elements (also known as spherical tesseroids; e.g. Anderson 1976) approximated by rectangular prisms (cf. section 3.1). Following the methodology by Grüninger (1990), Kuhn (2000) and Heck and Seitz (2007) the vertical extension of the prism is selected to be identical to the spherical tesseroid and the horizontal dimensions are obtained for first-order mass equivalence. In order to account for sphericity, the vertical centre line of a prism is aligned with the radial direction through the centre of the respective spherical tesseroid (e.g. Kuhn 2000, Heck and Seitz 2007). Furthermore, the prism edges are aligned along the local north-south, east-west and radial directions (e.g. along a local north oriented Cartesian coordinate system). In order to derive the gravitational potential and its first- and second-order derivatives we employ the analytical formulae for a rectangular prism provided by, e.g. Mader (1951), Nagy (1966), Nagy et al. (2000). We acknowledge also the possibility to employ the tesseroid formulae introduced

285 by Heck and Seitz (2007) and optimized by Grombein et al. (2013) as an alternative
286 computational approach (see also Deng et al. 2016).

3 Numerical Study

3.1 General

The goal of our numerical study is to carefully examine the Earth's topographic potential and first- and second-order derivatives using (i) rigorous topographic and (ii) approximate RET mass modelling (cf. sections 2.1 and 2.2). Particular focus will be placed on the differences in the respective gravitational functional between the two methods.

In the rigorous approach, each terrain type of the Earth2014 model suite (described in section 2.1) was (individually) forward modelled using the discretized Newtonian integration approach (section 2.3) and superimposed to obtain the gravitational effects of the complete topographic masses defined by Earth2014 (hereafter called Earth2014 masses). As approximate technique, following the methodology in section 2.2, for each terrain type of Earth2014 the mass components were compressed into RET masses in spherical approximation (hereafter called RET2014 masses, which, however, must not be confused with the precomputed Earth2014 RET-layer in planar approximation that is not utilized here), and forward modelled to yield the RET-induced gravitational effects. Finally, differences between both calculations were formed and analyzed, directly reflecting the RET approximation effect (cf. sections 3.2 to 3.4).

In all practical computations the Earth2014 and RET2014 models were used at 5 arc-min resolution. The globally distributed computation points were arranged at the center of each 5 arc-minute grid element. Three levels of computation heights were used:

(1) on the Earth's surface
(2) 3 km above the Earth's surface, and
(3) at a constant height of 250 km above the height reference surface (e.g. mean sphere in spherical approximation)

For the rigorous calculation, the Earth surface was represented by the Earth2014 component "SUR2014". It provides topographic heights of (dry) bedrock above MSL, zero heights (H = 0 m) over the oceans and lake heights over the major lakes. For land areas below MSL (e.g. parts of North Africa), H = 0 m was used too. In case of RET2014-based forward modelling, the Earth's surface is approximated by H_{RET}. As such the computation point heights are set to H_{RET} for RET2014 elevations greater than zero and H_{RET} = 0 m elsewhere. We acknowledge that an alternative approach could be the use of SUR2014 for both Earth2014- and RET2014-based forward modelling. However, this leads to computation points often located well above the

RET2014 surface, e.g. most notably over ice covered areas. This is why we did not consider this approach here.

To reduce computation times the 5 arc-minute resolution was used to model masses only in the vicinity around each computation point (i.e., 20 arc degree extension in both longitude and latitude, cf. Table 2) and a 15 arc-minute resolution was used to account for the global effect of the more distant masses. The 15 arc-minute resolution was obtained from the 5 arc-minute resolution by arithmetic averaging. This is common practice (e.g. Forsberg 1984, Kuhn 2000) and permitted due to the attenuation of gravity with distance. Table 2 details the spatial resolutions, extensions and mass elements used in this study.

Table 2: DEM resolutions, spatial extensions, and mass elements used for the discretised Newtonian integration. The spatial extensions are given as arc-distances along a parallel and meridian and define areas centred around each computation point.

Resolution	Extension	Mass Element
5′ × 5′	20° × 20°	Prism
15′ × 15′	Global	Prism

Due to the very high computational burden of our gravity forward modelling procedures, massive parallel computation was employed using Western Australia's supercomputer *Magnus* operated by the Pawsey Supercomputing Center. Magnus is a Cray XC40 system hosting Xeon E5-2690V3 "Haswell" processors running at 2.6 GHz, for a total of 35,712 cores, delivering in excess of 1 PetaFLOP of computing power (see https://www.pawsey.org.au/). For the computation the globally distributed computation points have been divided into 20 × 20 degree tiles, containing 56,700 points each, which were computed in parallel. The calculation required about 34,000 CPU hours (~3.9 years) for the rigorous modelling of the topography using Earth2014 and about 16,000 CPU hours (~1.8 years) when using RET2014. Using massive parallel computation allowed the processing of all tiles and functionals at the same time, thus the gravity forward modelling could effectively be performed in about one day.

3.2 Uncertainty Estimates

To provide uncertainty estimates for the 10 gravitational functionals obtained from discretized Newtonian integration (cf. section 2.3) we test our computation procedure by calculating the gravitational functionals induced by a spherical shell. The spherical shell has been selected with a mass density of ρ_0 and thickness of 6 km, thus representing a somewhat extreme case for global topographic masses.

Table 3: Uncertainty estimates for the 10 gravitational functional obtained through comparison with the analytically derived values of a spherical shell with a mass density of ρ_0 and thickness of 6 km. RMS and RMS_{rel} represent the root-mean-square values obtained from the globally distributed absolute and relative differences, respectively. Absolute differences are obtained by subtracting the analytically derived values from that obtained via Newtonian integration. Relative differences are obtained by dividing the absolute differences by the analytically derived values. Potential values have the unit m^2s^{-2}, first-order derivatives have the unit mGal (1 mGal = 1×10^{-5} ms^{-2}) and the second-order derivatives have the unit Eötvös (1 E = 1×10^{-9} s^{-2}). Note some outliers within a band of 5 degrees around the poles have been removed.

Functional	On shell(1)		3 km above shell		250 km above shell	
	RMS	RMS_{rel}	RMS	RMS_{rel}	RMS	RMS_{rel}
ΔV	1.178e-1	1.374e-6	1.179e-1	1.377e-6	1.151e-1	1.340e-6
Δg_φ	1.660e-1	n/a	1.660e-1	n/a	1.401e-2	n/a
Δg_λ	1.608e-6	n/a	1.208e-6	n/a	1.648e-6	n/a
Δg_r	1.462e-2	1.089e-5	1.462e-2	1.089e-5	4.703e-3	3.783e-6
$\Delta M_{\varphi\varphi}$	1.567e-1	7.452e-2	9.429e-4	4.491e-4	7.578e-5	4.045e-5
$\Delta M_{\lambda\lambda}$	1.733e-1	8.241e-2	9.649e-3	4.596e-3	2.806e-5	1.498e-5
ΔM_{rr}	2.097e-1	4.986e-2	8.958e-2	2.133e-3	4.848e-5	1.294e-5
$\Delta M_{\varphi\lambda}$	3.860e-6	n/a	3.249e-7	n/a	3.023e-6	n/a
$\Delta M_{\varphi r}$	4.148e-1	n/a	1.062e-1	n/a	2.910e-5	n/a
$\Delta M_{\lambda r}$	3.756e-6	n/a	2.736e-7	n/a	1.151e-7	n/a

(1)For gravitational potential and its first-order derivatives computation points are located on the spherical shell while they are 1 m above the spherical shell for the second-order derivatives.

The calculation of the gravitational functionals has been performed for a global 5-arc-minute by 5-arc-minute grid at the three elevations listed in section 3.1. Differences between the numerical calculation results and the analytically determined values (see e.g. Makhloof and Ilk

2008a) are taken as a measure for the uncertainty. Based on a global distribution of the computation points, Table 3 lists the RMS values of these differences. In addition Table 3 lists the RMS values for the relative differences (RMS_{rel} in Table 3) where the (absolute) differences at each computation point have been divided by the analytically determined values.

For computation points located either on or 3 km above the shell all RMS values of the differences are well below 1.0 $m^2s^{-2}1$, 0.1 mGal (1 mGal = 1×10^{-5} ms^{-2}) and 1 Eötvös (1 E = 1×10^{-9} s^{-2}), for the gravitational potential, first- and second-order derivatives, respectively. Except for the gravitational potential, the RMS values reduce by several orders of magnitude when evaluating 250 km above the shell. Furthermore, all RMS values of the relative differences are significantly lower than the RMS values of the absolute differences. It should be noted that the calculation of the second-order derivatives are not defined on interfaces of density discontinuity (e.g. at the Earth's surface) but depend on the direction from which the interface is approached (e.g. Nagy et al. 2000, Makhloof and Ilk 2008a). This is why we have selected the computation points to be located 1 m above the Earth's surface, even though in this study we always approach the interface (e.g. prism face) from the 'exterior'.

Considering that all RMS values shown in Table 3 are significantly lower than the differences between the rigorous modelling of the Earth's topography and compressed RET presented in sections 3.3 to 3.5 we are confident that these differences are due to RET approximation errors rather than discretization errors in the Newtonian integration. Also note such test represents an extreme situation and actual results will have a much smaller uncertainty when using the concept of spherical terrain corrections, thus only residual masses are considered and the gravitational effect of the spherical shell is calculated analytically (e.g. Makhloof and Ilk (2008a).

3.3 Topographic Potential

We computed the Earth's topographic potential based on the topographic masses given by the Earth2014 model and corresponding RET2014 masses using discretized Newtonian integration. The computations have been performed on the Earth's surface, 3 km above the Earth's surface and at a constant height of 250 km. As the results for the topographic potential for Earth2014 and RET2014 are very similar we only show that of Earth2014 in Figure 4 (upper row), and the differences between the rigorous and approximate computation (Figure 4, lower row). Further we only show the results on the Earth's surface and at the height of 250 km as that for 3 km above the Earth's surface is very similar to that on the Earth's surface. The

corresponding statistical values for Earth2014, RET2014 and differences are listed in Table 4. The topographic potential is dominated by the large mass deficit of the ocean masses causing large negative values over deep ocean basins, most notably the Pacific Ocean, and a strongly negative global mean value of about -19,544 m^2s^{-2} at the surface (cf. Table 4). The strong negative values are reduced over areas with considerable masses above MSL representing a mass surplus, most notably over the Himalaya. Due to the relatively slow attenuation of the gravitational potential with distance its spatial distribution is rather smooth and closely related for the three elevation levels considered.

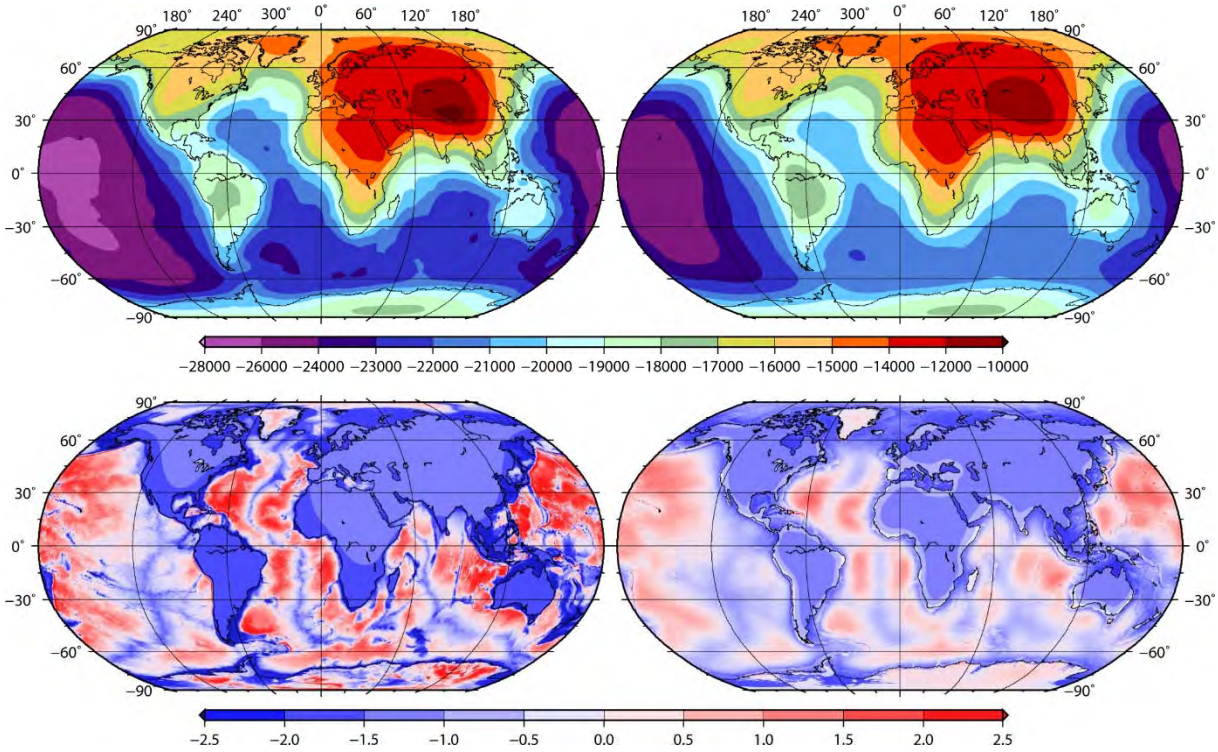

Figure 4: Top: Topographic potential of Earth2014 evaluated on the Earth's surface (top left) and at the constant height of 250 km (top right). Bottom: Difference between topographic potential of Earth2014 and RET2014 for the corresponding elevations in the top plots. Units in m^2s^{-2}.

Differences between the topographic potential generated by the Earth2014 and corresponding RET2014 masses are displayed in Figure 4 (lower row). For all three elevations considered larger differences are present over deep ocean and ice covered areas with maximum values over deep ocean trenches (e.g. Mariana Trench) for computation points located either on or 3 km above the Earth's surface. This immediately shows the effect of the RET2014 masses considerably changing (compressing) the topographic masses over ocean and ice covered areas. On a global scale the impact of major lakes and areas of dry bedrock below MSL have only a very small impact on the gravitational potential and are not visible in Figure 4, though can become important for local modelling (Tenzer et al. 2016).

Table 4: Statistical values for the topographic potential of Earth2014 (δV_{Top}), RET2014 (δV_{RET}) and differences ($\Delta V_{Top\text{-}RET}$) evaluate on the Earth's surface (index S), 3 km above the Earth's surface (index 3km) and at the constant height of 250 km (index 250km). Units in m^2s^{-2}. Relative difference represents the range in differences in relation to the range in signal.

Functional	Min	Max	Mean	Stdv	Relative
$\delta V_{Top,S}$	-26,667.603	-9,289.620	-19,544.552	3,819.626	n/a
$\delta V_{RET,S}$	-26,669.720	-9,288.413	-19,554.026	3,820.198	n/a
$\Delta V_{Top\text{-}RET,S}$	-3.981	9.512	-0.526	1.266	0.078%
$\delta V_{Top,3km}$	-26,649.500	-9,304.530	-19,536.041	3,814.817	n/a
$\delta V_{RET,3km}$	-26,651.617	-9,303.324	-19,535.516	3,815.387	n/a
$\Delta V_{Top\text{-}RET,3km}$	-3.758	8.356	-0.525	1.246	0.070%
$\delta V_{Top,250km}$	-25,305.252	-10,223.340	-18,859.787	3,485.500	n/a
$\delta V_{RET,250km}$	-25,306.497	-10,222.245	-18,859.235	3,458.941	n/a
$\Delta V_{Top\text{-}RET,250km}$	-4.610	3.818	-0.552	0.808	0.056%

Maximum differences reach values of almost 10 m^2s^{-2} for computation points located on the Earth's surface and 5 m^2s^{-2} at the height of 250 km, which correspond to effects on the geoid height of ~1 m and ~0.5 m, respectively. In relation to the magnitude of the global signal the differences are relatively small as can be seen by comparison of the range in signal and range of differences. As a measure to describe global relative differences we use the percentage value taken up by the range in differences in relation to the range in signal (cf. Table 4), which provides a global measure on the relative importance of the differences or the suitability of replacing rigorous topographic by RET masses. For the topographic potential the global relative differences remain below 0.1 % for all three elevations considered, thus it could be argued that the RET compression may be acceptable for some global studies relying on the gravitational potential.

While it is expected that differences are largest over areas where the Earth2014 masses have been compressed to RET2014 masses, it is interesting to note that there is also some impact (largely as a bias) over areas with dry bedrock above MSL where the Earth2014 and RET2014 masses are identical. For all three elevation cases, the impact can reach more than 1 m^2s^{-2} (e.g. > 0.1 m geoid height change) at locations over land several thousand kilometers away from the coastline. Given that the gravitational potential at some location is generated by the accumulated gravitation of all masses around the globe, the cause of this bias-like effect becomes evident.

3.4 First-Order Derivatives of the Topographic Potential

First-order derivatives of the topographic potential (cf. section 3.3) representing the vector components $\delta g_\varphi, \delta g_\lambda, \delta g_r$ have been computed using discretized Newtonian integration and are shown in Figure 5 for Earth2014. Due to the same reason as for the topographic gravitational potential we only show the results for Earth2014 masses on the Earth's surface and at the height of 250 km in Figure 5. Representing the gravitational acceleration in north-south and east-west directions, the vector components δg_φ and δg_λ, respectively, show high magnitudes at places with considerable elevation changes in north-south and east-west directions.

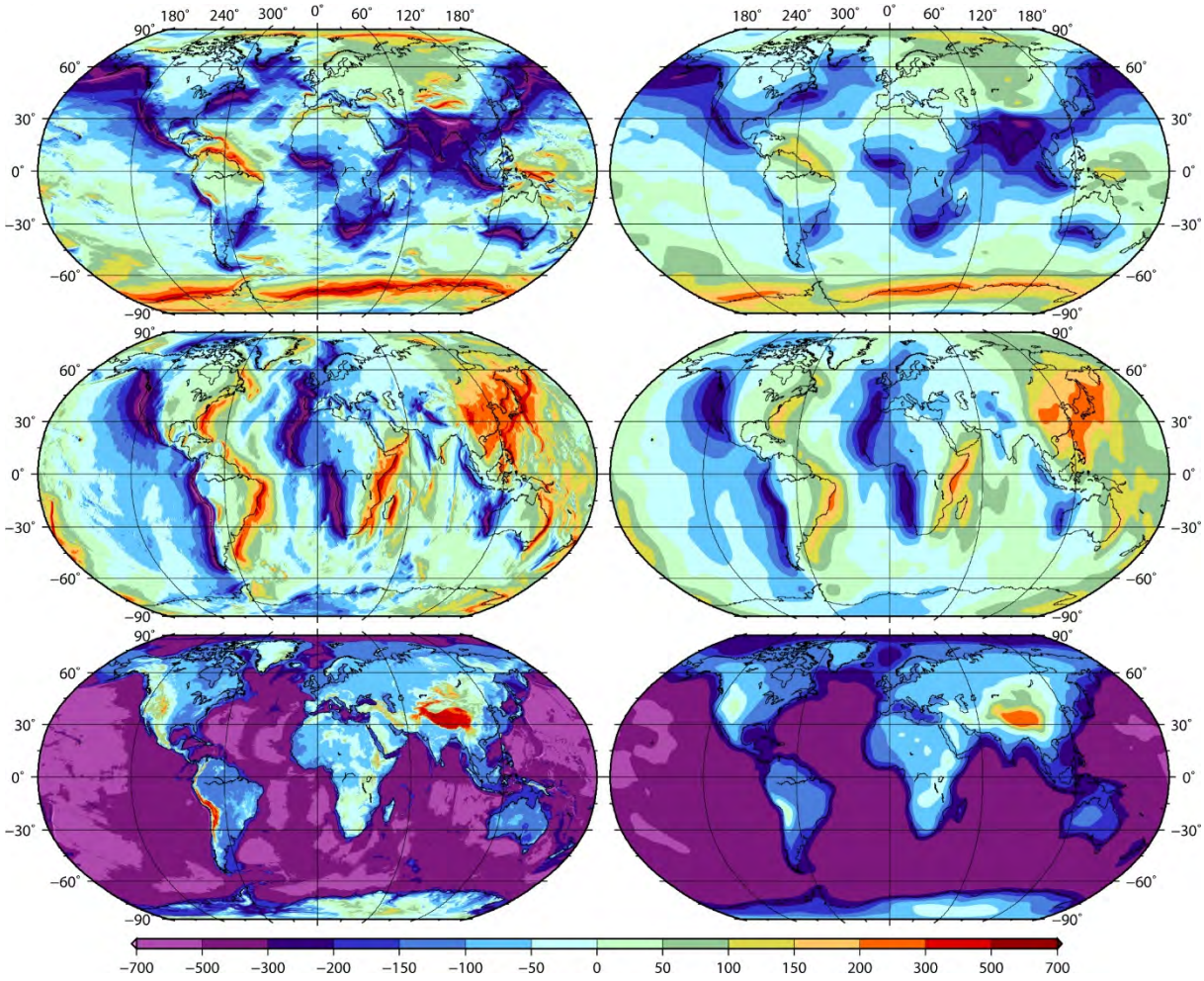

Figure 5: First-order derivatives of the topographic potential of Earth2014 evaluated on the Earth's surface (left column) and at the constant height of 250 km (right column). From top to bottom the figures in each column represent $\delta g_\varphi, \delta g_\lambda, \delta g_r$. Units in mGal (1 mGal = 1×10^{-5} ms^{-2}).

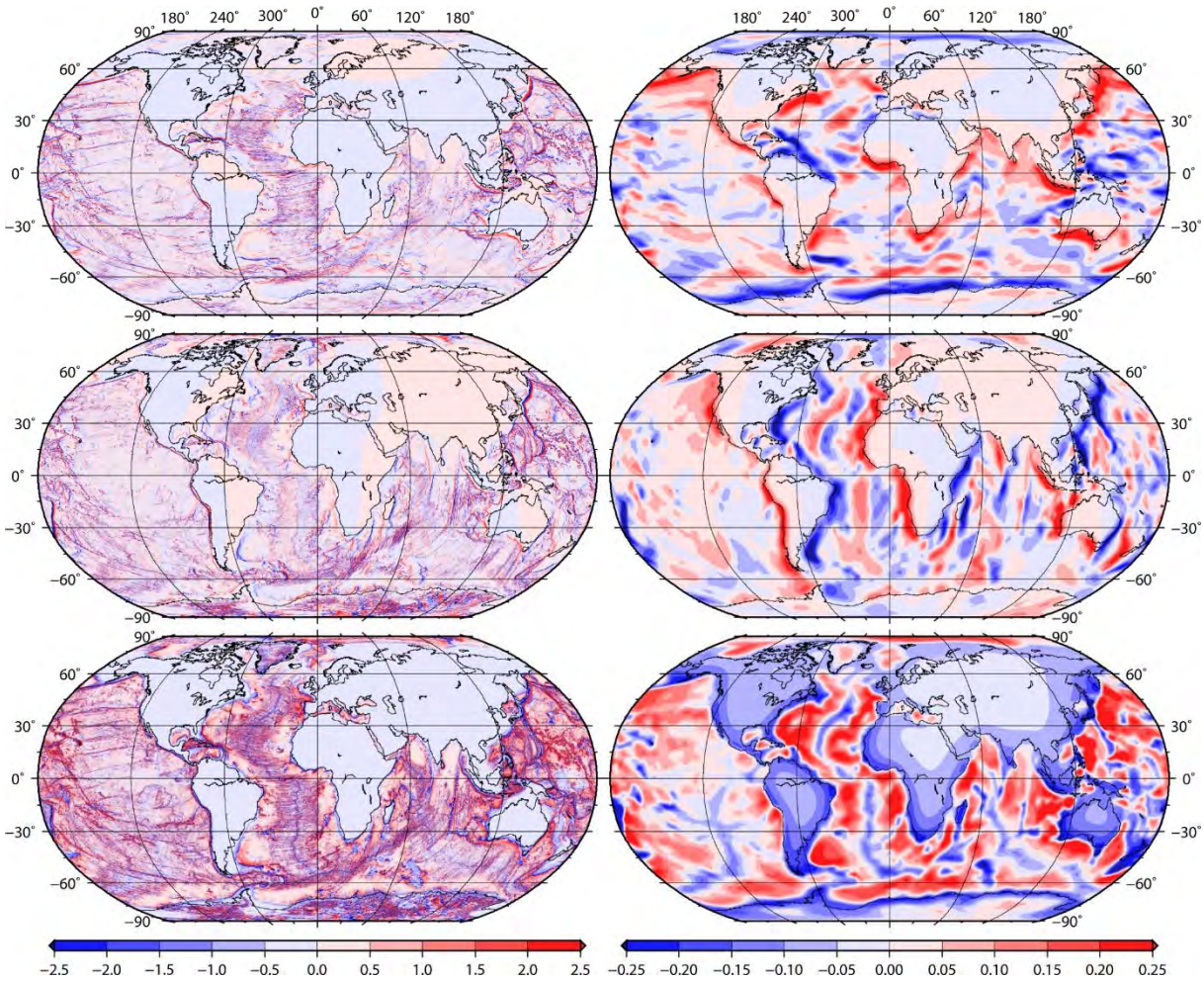

459

460 **Figure 6:** Differences of the first-order derivatives of the topographic potential between Earth2014 (cf. Figure 5)
461 and RET2014 evaluated on the Earth's surface (left column) and at the constant height of 250 km (right column).
462 From top to bottom the figures in each column represent $\Delta g_\varphi, \Delta g_\lambda, \Delta g_r$. Units in mGal (1 mGal = 1×10^{-5} ms^{-}
463 ^{2}).
464

Table 5: Statistical values for the first-order derivatives of the topographic potential of Earth2014 (δg^{Top}), RET2014 (δg^{RET}) and differences ($\Delta g^{Top\text{-}RET}$) evaluated on the Earth's surface (index S), 3 km above the Earth's surface (index 3km) and at the constant height of 250 km (index 250km). Units in mGal (10^{-5} ms^{-2}). Relative difference represents the range in differences in relation to the range in signal.

Functional	Min	Max	Mean	Stdv	Relative
$\delta g_{\varphi}^{Top,S}$	-852.664	531.460	-10.256	131.097	n/a
$\delta g_{\lambda}^{Top,S}$	-847.543	699.056	0.242e-2	114.375	n/a
$\delta g_{r}^{Top,S}$	-798.309	627.183	-283.843	204.191	n/a
$\delta g_{\varphi}^{RET,S}$	-852.659	533.620	-10.246	131.236	n/a
$\delta g_{\lambda}^{RET,S}$	-847.786	712.766	0.232e-3	114.559	n/a
$\delta g_{r}^{RET,S}$	-831.766	627.223	-283.828	204.505	n/a
$\Delta g_{\varphi}^{Top-RET,S}$	-20.868	22.189	-0.101e-1	0.731	3.111%
$\Delta g_{\lambda}^{Top-RET,S}$	-23.382	21.555	0.219e-2	1.069	2.906%
$\Delta g_{r}^{Top-RET,S}$	-37.210	58.407	-0.157e-1	1.993	6.708%
$\delta g_{\varphi}^{Top,3km}$	-838.465	515.293	-10.289	130.422	n/a
$\delta g_{\lambda}^{Top,3km}$	-833.413	666.735	0.288e-2	113.603	n/a
$\delta g_{r}^{Top,3km}$	-770.359	596.400	-283.563	202.899	n/a
$\delta g_{\varphi}^{RET,3km}$	-838.460	518.836	-10.276	130.604	n/a
$\delta g_{\lambda}^{RET,3km}$	-834.031	681.797	0.224e-3	113.797	n/a
$\delta g_{r}^{RET,3km}$	-796.849	596.440	-283.541	203.166	n/a
$\Delta g_{\varphi}^{Top-RET,3km}$	-17.125	19.472	-0.129e-1	0.824	2.703%
$\Delta g_{\lambda}^{Top-RET,3km}$	-19.209	17.144	0.266e-2	0.920	2.423%
$\Delta g_{r}^{Top-RET,3km}$	-24.045	27.782	-0.226e-1	1.365	3.792%
$\delta g_{\varphi}^{Top,250km}$	-337.302	248.399	-13.211	95.433	n/a
$\delta g_{\lambda}^{Top,250km}$	-297.739	279.416	-0.294e-5	82.576	n/a
$\delta g_{r}^{Top,250km}$	-524.667	300.110	-264.658	154.115	n/a
$\delta g_{\varphi}^{RET,250km}$	-337.204	248.592	-13.208	95.475	n/a
$\delta g_{\lambda}^{RET,250km}$	-297.940	279.847	-0.278e-5	82.612	n/a
$\delta g_{r}^{RET,250km}$	-524.855	300.150	-264.648	154.169	n/a
$\Delta g_{\varphi}^{Top-RET,250km}$	-0.388	0.408	-0.309e-2	0.744	0.136%
$\Delta g_{\lambda}^{Top-RET,250km}$	-0.473	0.354	-0.159e-6	0.696e-1	0.143%
$\Delta g_{r}^{Top-RET,250km}$	-0.300	0.446	0.990e-2	0.106	0.090%

The vector component δg_r instead is dominated by large negative values over the ocean areas and positive values over areas with high elevations above MSL (e.g. Himalaya). The latter component is the classical topographic correction in spherical approximation used to derive complete Bouguer gravity anomalies (e.g. Kuhn et al. 2009). Like the topographic potential also δg_r is dominated by the mass deficiency of the oceans introducing a large negative bias (cf. Table 5) visible by largely negative values over continental areas (except areas with very high elevations).

Differences between the first-order derivatives of the topographic potential generated by the Earth2014 and RET2014 masses are displayed in Figure 6. These are mostly present over ocean and ice covered areas with maximum magnitudes on the Earth's surface of about 20 mGal for δg_φ and δg_λ and almost 60 mGal for δg_r (cf. Table 5). In relation to the signal the range of the differences takes up 3.1%, 2.9% and 6.7% when compared to the range of $\delta g_\varphi, \delta g_\lambda$ and δg_r, respectively, thus demonstrate a considerable difference when using RET instead of rigorous topographic masses. Similar results are obtained at an elevation of 3 km, though with slightly reduced values (cf. Table 5). At the elevation of 250 km differences are considerably smaller with maximum magnitudes around 0.4 mGgal for all vector components $\delta g_\varphi, \delta g_\lambda$ and δg_r. The relative significance of the differences is also smaller and takes up values around 0.1% when comparing the range of the differences to that of $\delta g_\varphi, \delta g_\lambda$ and δg_r. As for the topographic potential also the first-order derivatives exhibit larger differences over areas of dry bedrock above MSL where Earth2014 and RET2014 masses are identical. For computation points on or 3 km above the Earth's surface these differences are mostly confined to coastal areas (e.g. impact from the compressed ocean masses) with differences below 1 μGal well inside a continent. However, when evaluating at an elevation of 250 km (cf. Figure 6) there is considerable influence introducing biases of almost 100 μGal well inside a continent and even higher biases closer to the coastline.

3.5 Second-Order Derivatives of the Topographic Potential

Relevant to satellite gradiometry such as the GOCE mission (Rummel et al. 2011), airborne gradiometry (Douch et al. 2015), or torsion balance measurements (Völgyesi 2001), we also computed the second-order derivatives of the Earth's topographic potential based on the topographic masses given by Earth2014 and RET2014 masses using discretized Newtonian

integration. The nine second-order derivatives are the elements of the symmetric Eötvös tensor of which five elements are independent of each other as the condition $\delta V_{\varphi\varphi} + \delta V_{\lambda\lambda} = -\delta V_{rr}$ holds (cf. section 2.3). Here we calculate the three diagonal components $\delta V_{\varphi\varphi}$, $\delta V_{\lambda\lambda}$, δV_{rr} and the three off-diagonal component $\delta V_{\varphi\lambda}$, $\delta V_{\varphi r}$, $\delta V_{\lambda r}$. We consider three levels of elevation. The computation points were elevated by 1 m above the Earth's surface (this is in contrast to Sect. 3.3 and 3.4), 3 km above the Earth's surface and at the constant height of 250 km above the reference sphere. As the second-order derivatives are not defined on interfaces of density discontinuity we do not evaluate directly on the Earth's surface but 1 m above it so to avoid possible singularities (cf. 3.2).

The second-order derivatives are illustrated in Figures 7 and 8 for Earth2014. Again we only display the results for Earth2014 masses as that for RET2014 masses are very similar. The diagonal components $\delta V_{\varphi\varphi}$ and $\delta V_{\lambda\lambda}$ represent the gravity gradients in north-south and east-west directions, respectively, and as such show larger values at places with considerable height changes in north-south and east-west directions, respectively. The diagonal component δV_{rr} represents the gravity gradient in radial direction and shows larger values over places with high elevations, most notably over the Himalaya and Andes (cf. Figure 7). The remaining three off-diagonal components $\delta V_{\varphi\lambda}$, $\delta V_{\varphi r}$, and $\delta V_{\lambda r}$ are the 'cross' gravity gradients where $\delta V_{\varphi r}$, and $\delta V_{\lambda r}$ are somewhat dominated by the derivative in the horizontal directions, respectively, and $\delta V_{\varphi\lambda}$ partly cancels (see much reduced signal in Figure 8 and Table 6). Based on the diagonal components $\delta V_{\varphi\varphi}$, $\delta V_{\lambda\lambda}$ and δV_{rr} we have tested the Laplace equation $\delta V_{\varphi\varphi} + \delta V_{\lambda\lambda} + \delta V_{rr} = 0$, which is satisfied in this study at the 10^{-10} E level (min/max: $\pm 7\times10^{-10}$ E; mean: 3.2×10^{-14} E; RMS: 1.3×10^{-10} E) for Earth2014 when evaluating 1 m above the Earth's surface. Very similar levels of agreement are obtained when evaluating either 3 km above the Earth's surface or at an elevation of 250km.

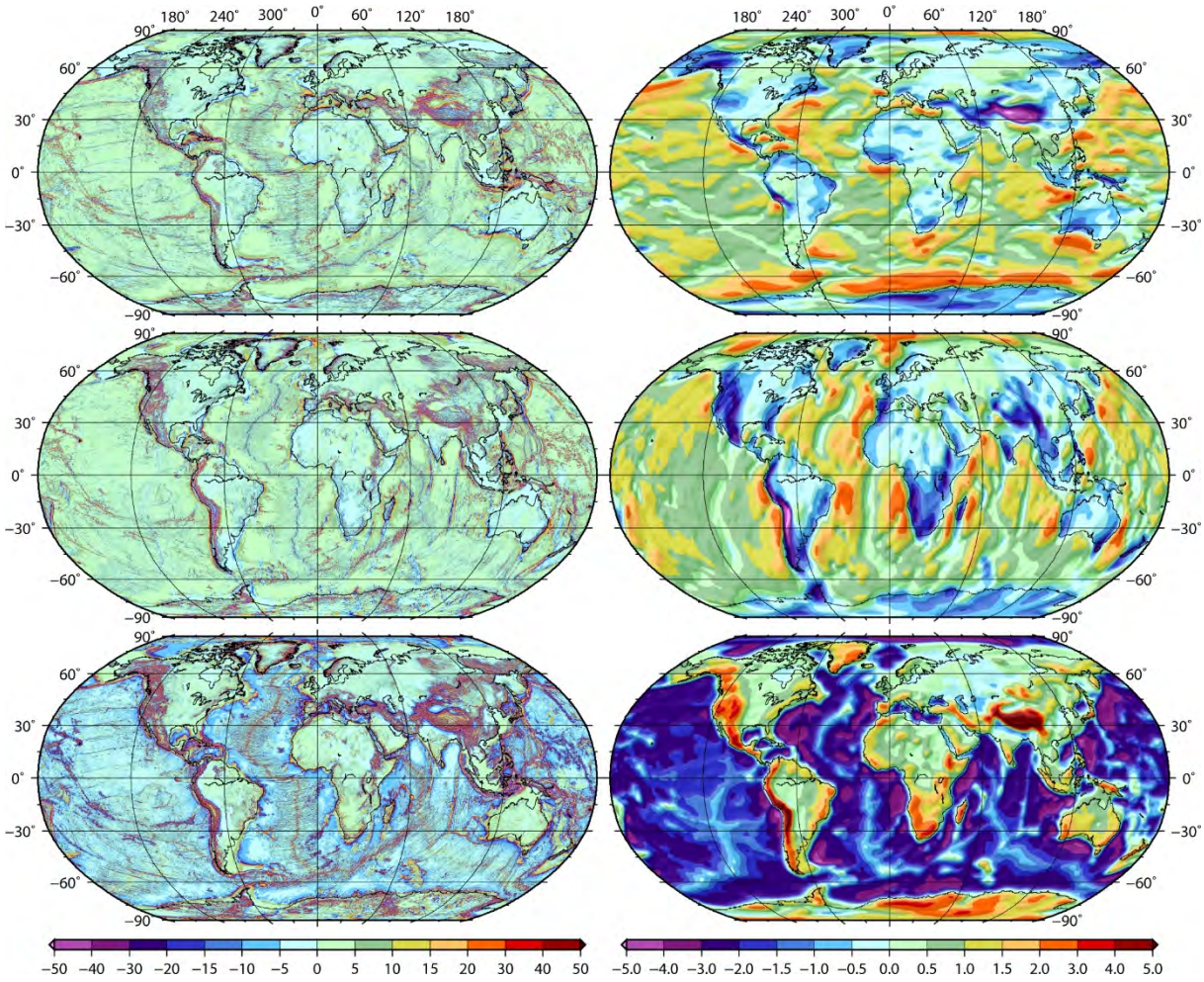

528

529 **Figure 7:** Second-order derivatives (diagonal elements of the Eötvös tensor) of the topographic potential of
530 Earth2014 evaluated on the Earth's surface (left column) and at the constant height of 250 km (right column).
531 From top to bottom the figures represent $\delta V_{\varphi\varphi}, \delta V_{\lambda\lambda}, \delta V_{rr}$. Units in Eötvös (1 E = 1×10^{-9} s^{-2}).

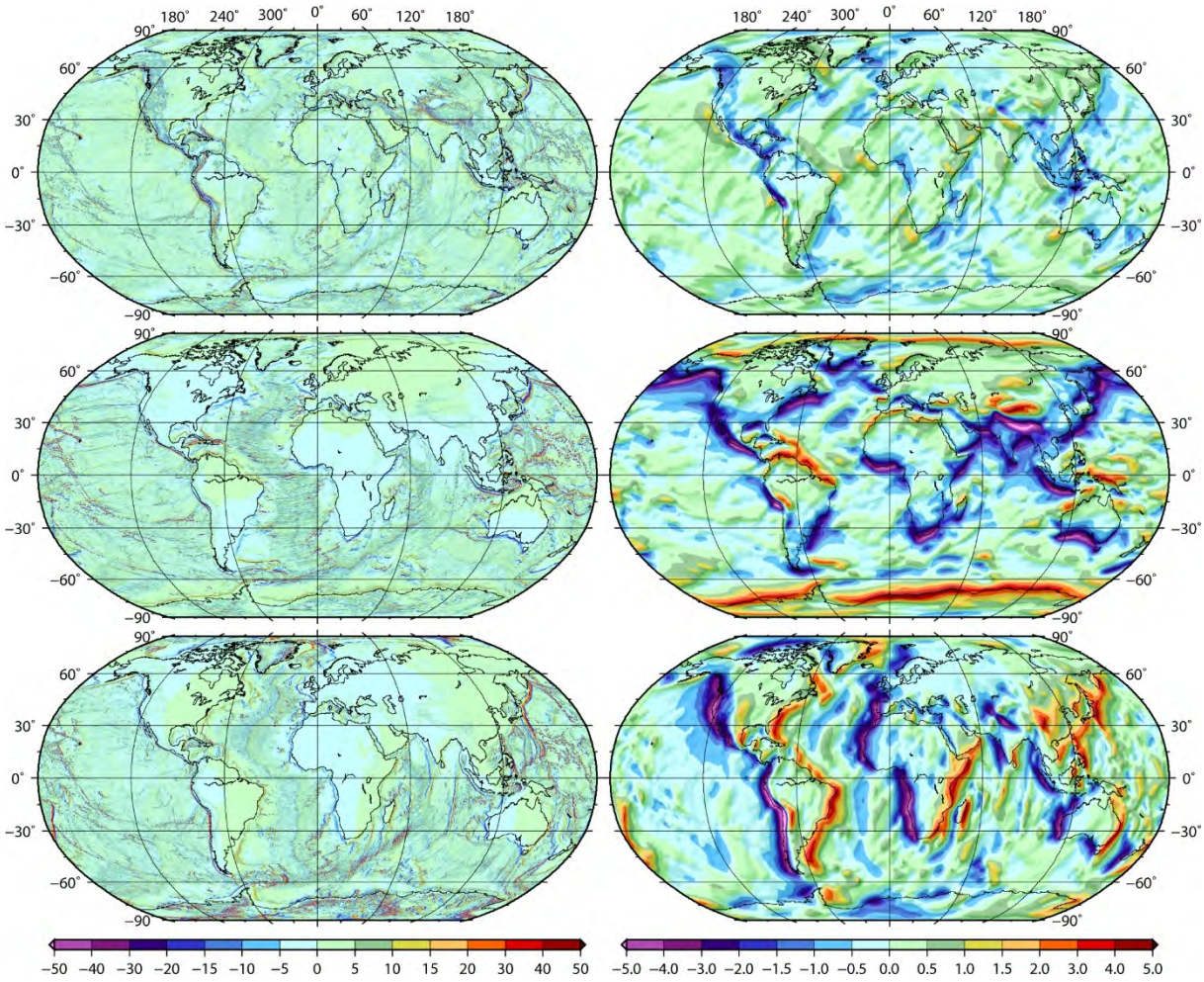

532

533 **Figure 8:** Second derivatives of the topographic potential (off-diagonal elements of the Eötvös tensor) of
534 Earth2014 evaluated on the Earth's surface (left column) and at the constant height of 250 km (right column).
535 From top to bottom the figures represent $\delta V_{\varphi\lambda}$, $\delta V_{\varphi r}$, $\delta V_{\lambda r}$. Units in Eötvös (1 E = 1×10^{-9} s^{-2}).

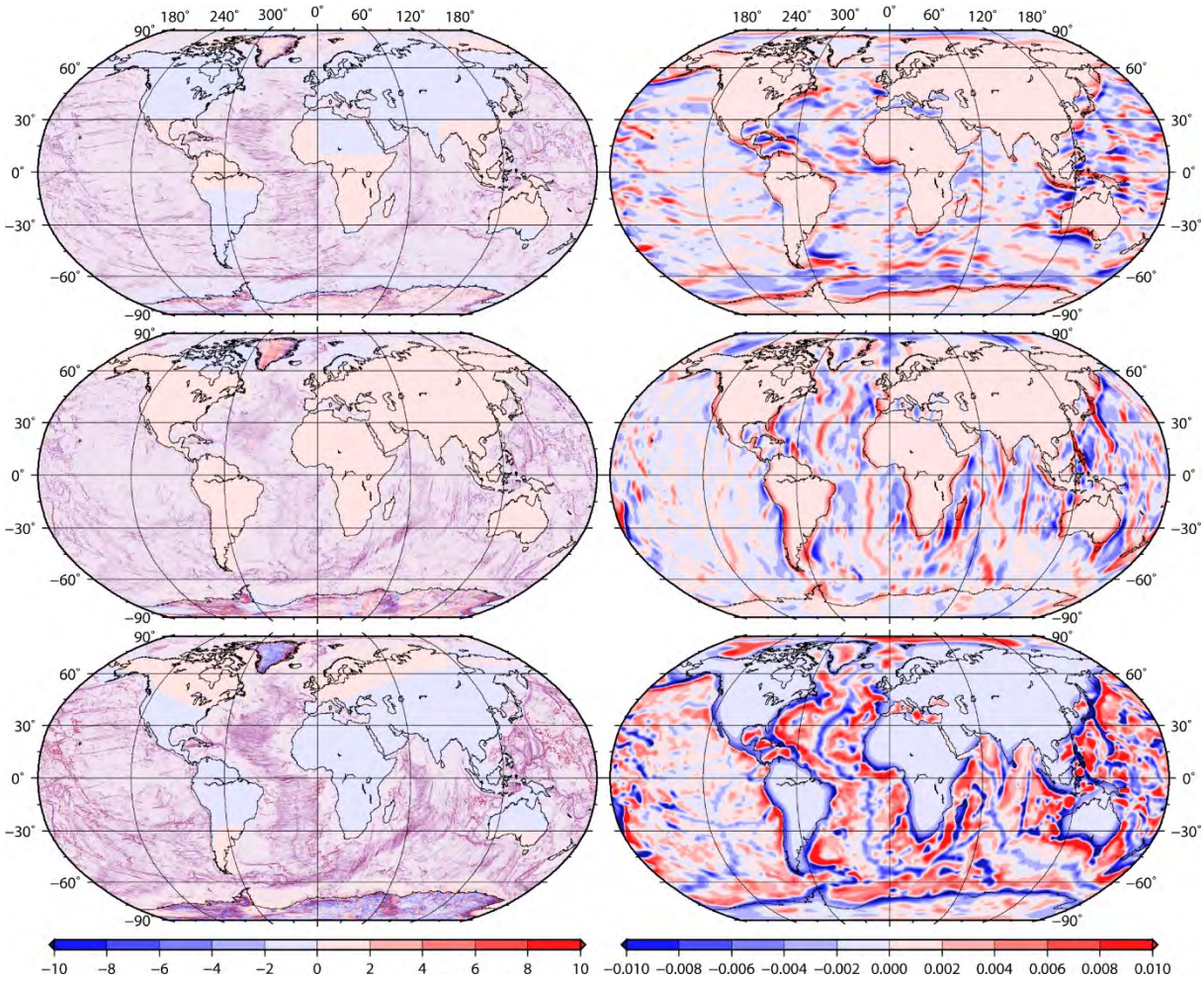

536

537 **Figure 9:** Difference between the second-order derivatives of the topographic potential (diagonal elements of the
538 Eötvös tensor) of Earth2014 and RET2014 evaluated on the Earth's surface (left column) and at the constant
539 height of 250 km (right column). From top to bottom the figures represent $\Delta V_{\varphi\varphi}$, $\Delta V_{\lambda\lambda}$, ΔV_{rr}. Units in Eötvös
540 (1 E = 1×10^{-9} s^{-2}).

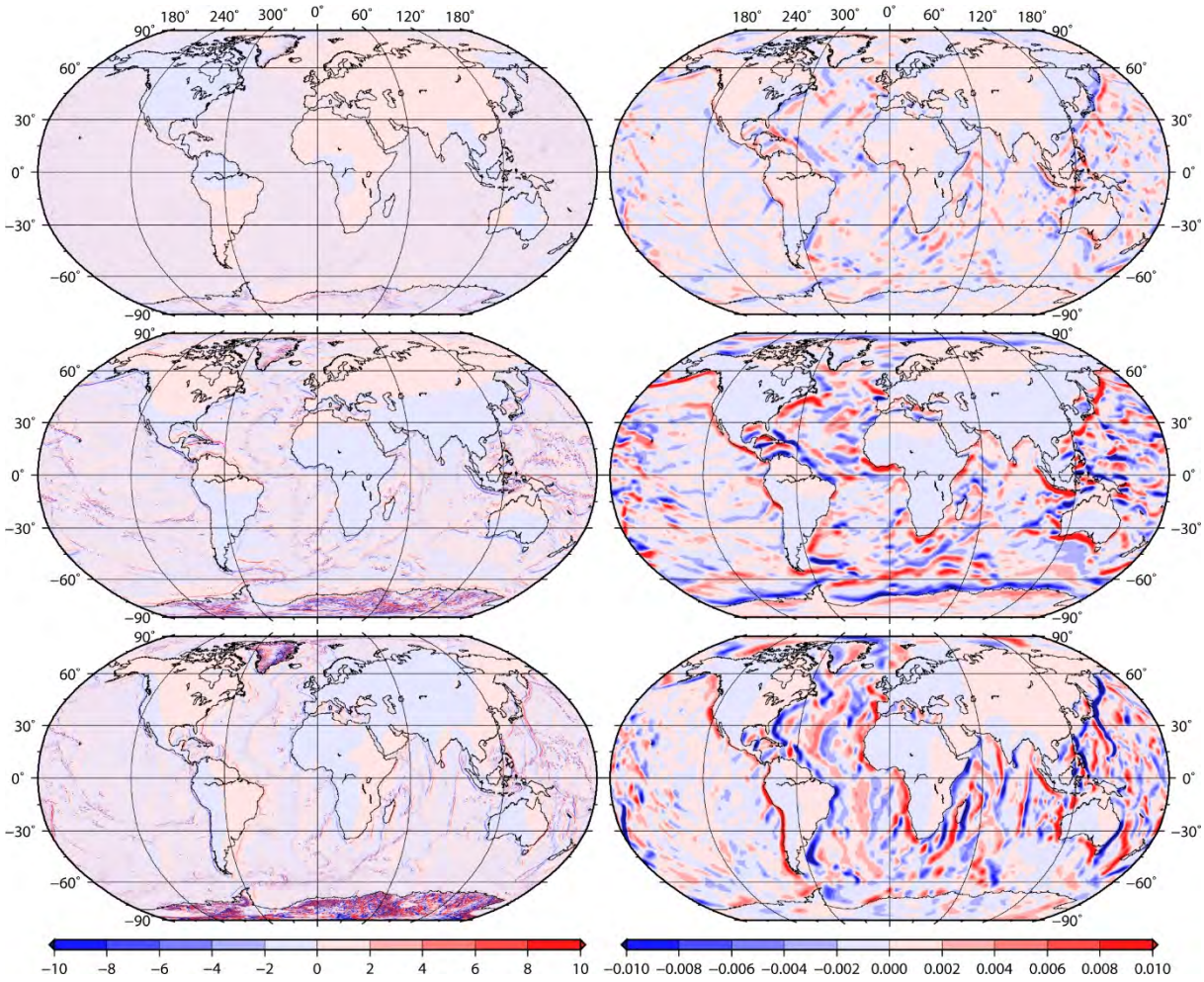

Figure 10: Difference between the second-order derivatives of the topographic potential (diagonal elements of the Eötvös tensor) of Earth2014 and RET2014 evaluated on the Earth's surface (left column) and at the constant height of 250 km (right column). From top to bottom the figures represent $\Delta V_{\varphi\lambda}$, $\Delta V_{\varphi r}$, $\Delta V_{\lambda r}$. Units in Eötvös (1 E = 1×10^{-9} s^{-2}).

Table 6: Statistical values for the second-order derivatives of the topographic potential of Earth2014 (δV^{Top}), RET2014 (δV^{RET}) and differences ($\Delta V^{Top\text{-}RET}$) evaluated 1 m above the Earth's surface (left part), 3 km above the Earth's surface (middle part) and at the constant height of 250 km (right part). Units in Eötvös (1E = 10^{-9} s^{-2}). Relative difference represents the range of differences in relation to the range in signal.

	1 m above the Earth's surface					3 km above the Earth's surface				
Functional	**Min**	**Max**	**Mean**	**Stdv**	**Rel.**	**Min**	**Max**	**Mean**	**Stdv**	**Rel.**
$\delta V^{Top}_{\varphi\varphi}$	-256.940	220.888	0.440	11.604	n/a	-166.158	190.693	0.498	8.335	n/a
$\delta V^{Top}_{\lambda\lambda}$	-441.100	520.047	0.436	13.695	n/a	-179.855	232.671	0.447	8.252	n/a
δV^{Top}_{rr}	-518.868	491.892	-0.877	20.559	n/a	-236.131	302.660	-0.945	13.492	n/a
$\delta V^{Top}_{\varphi\lambda}$	-85.475	84.391	0.272e-3	4.944	n/a	-79.351	74.630	0.821e-3	4.092	n/a
$\delta V^{Top}_{\varphi r}$	-104.681	100.045	0.031	5.516	n/a	-129.686	108.387	0.149	7.229	n/a
$\delta V^{Top}_{\lambda r}$	-294.080	279.252	-0.015	8.352	n/a	-148.971	178.479	0.170e-3	8.221	n/a
$\delta V^{RET}_{\varphi\varphi}$	-256.938	220.888	0.446	12.288	n/a	-166.490	190.693	0.508	8.974	n/a
$\delta V^{RET}_{\lambda\lambda}$	-401.555	464.933	0.383	14.402	n/a	-184.690	232.671	0.460	8.834	n/a
δV^{RET}_{rr}	-433.208	491.891	-0.829	21.703	n/a	-236.131	305.834	-0.968	14.477	n/a
$\delta V^{RET}_{\varphi\lambda}$	-86.091	85.538	-0.176e-4	5.039	n/a	-79.351	74.798	0.913e-3	4.322	n/a
$\delta V^{RET}_{\varphi r}$	-85.504	84.730	0.032	4.309	n/a	-133.278	113.845	0.149	7.350	n/a
$\delta V^{RET}_{\lambda r}$	-174.828	201.348	0.639e-4	6.338	n/a	-149.892	194.949	0.135e-4	8.701	n/a
$\Delta V^{Top-RET}_{\varphi\varphi}$	-52.798	46.295	-0.005	1.958	20.74%	-27.983	24.704	-0.010	1.159	14.76%
$\Delta V^{Top-RET}_{\lambda\lambda}$	-144.220	219.643	0.053	2.793	37.86%	-54.182	26.555	-0.013	1.109	19.57%
$\Delta V^{Top-RET}_{rr}$	-218.725	145.405	-0.048	3.815	36.02%	-40.005	68.793	0.022	1.844	20.19%
$\Delta V^{Top-RET}_{\varphi\lambda}$	-18.292	16.330	0.290e-3	0.638	20.38%	-9.004	7.823	-0.912e-4	0.401	10.93%
$\Delta V^{Top-RET}_{\varphi r}$	-48.042	59.345	-0.002	1.973	52.45%	-14.620	11.883	0.003	0.506	11.13%
$\Delta V^{Top-RET}_{\lambda r}$	-330.537	299.937	-0.015	5.270	109.97%	-33.608	32.986	0.156e-3	0.994	20.34%

Functional	**Constant height of 250 km**				
$\delta V^{Top}_{\varphi\varphi}$	-5.403	3.244	0.399	0.980	n/a
$\delta V^{Top}_{\lambda\lambda}$	-6.550	3.159	0.309	0.951	n/a
δV^{Top}_{rr}	-4.632	7.052	-0.709	1.699	n/a
$\delta V^{Top}_{\varphi\lambda}$	-3.402	1.829	-0.625e-7	0.422	n/a
$\delta V^{Top}_{\varphi r}$	-6.761	4.701	0.082	1.135	n/a
$\delta V^{Top}_{\lambda r}$	-7.625	4.586	-0.207	1.004	n/a
$\delta V^{RET}_{\varphi\varphi}$	-5.403	3.255	0.399	0.981	n/a
$\delta V^{RET}_{\lambda\lambda}$	-6.555	3.172	0.310	0.952	n/a
δV^{RET}_{rr}	-4.653	7.055	-0.709	1.701	n/a
$\delta V^{RET}_{\varphi\lambda}$	-3.406	1.837	0.470e-8	0.423	n/a
$\delta V^{RET}_{\varphi r}$	-6.760	4.709	0.082	1.136	n/a
$\delta V^{RET}_{\lambda r}$	-7.639	4.607	0.289e-7	1.006	n/a
$\Delta V^{Top-RET}_{\varphi\varphi}$	-0.020	0.016	0.148e-4	0.002	0.41%
$\Delta V^{Top-RET}_{\lambda\lambda}$	-0.020	0.019	-0.648e-4	0.002	0.40%
$\Delta V^{Top-RET}_{rr}$	-0.021	0.025	0.501e-4	0.004	0.39%
$\Delta V^{Top-RET}_{\varphi\lambda}$	-0.008(*)	0.015	-0.672e-7	0.001	0.44%
$\Delta V^{Top-RET}_{\varphi r}$	-0.022	0.019	-0.740e-4	0.003	0.36%
$\Delta V^{Top-RET}_{\lambda r}$	-0.027(*)	0.052	-0.236e-6	0.003	0.65%

(*)Some outliers close to the poles have been removed.

552 Like for the first-order derivatives, differences between the second-order derivatives of the
553 topographic potential generated by Earth2014 and RET2014 masses are mostly present over
554 ocean and ice covered areas (cf. Figures 9 and 10). When evaluating 1 m above the Earth's
555 surface differences can reach several hundred Eötvös which are as large as the signal itself (cf.
556 Table 6). This is verified by the percentages of the ranges in differences in relation to the
557 ranges of the signal with values between 20% for $\delta V_{\varphi\lambda}$ and over 100% for $\delta V_{\lambda r}$. Thus in this
558 case RET2014 masses should clearly not be used as an approximation for the actual
559 topographic masses. This is not surprising considering the second-order derivatives strongly
560 amplify higher frequencies of the topographic potential. Differences over continental areas are
561 rather small instead, thus there is minimal influence from the compressed ocean masses.
562 Differences are still at a considerable level albeit reduced, when evaluating at an elevation of
563 3 km above the Earth's surface. In this case the percentage values of the relative differences
564 range between 11% and 20% (cf. Table 6).
565
566 At an elevation of 250 km both signal and differences are becoming increasingly smaller, which
567 is due to the attenuation of the second-order derivative with the cubed distance. In this case
568 the signal reaches maximum levels of less than ±10 E, which is consistent with estimates in
569 Wild-Pfeiffer (2008) and Eshagh (2009b). Maximum differences are now over two orders of
570 magnitude smaller than the signal as demonstrated by the percentage values ranging between
571 0.35% and 0.65% (cf. Table 6). Again, these values are consistent with those presented in
572 Grombein et al. (2010) with minor differences being likely due to the use of different
573 topography data. Furthermore, there is considerable influence on continental areas when
574 evaluating at the elevation of 250 km introducing biases of several mE in coastal areas (cf.
575 Figures 9 and 10) but reduce significantly for locations further away from the coast to levels
576 below 0.01 – 0.1 mE.
577
578 **4 Discussion and Conclusions**
579 Comparison between Earth2014 topographic and RET2014 masses revealed considerable
580 differences when used to derive the gravitational potential and its first- and second-order
581 derivatives. This holds for various elevation levels for the computation points with
582 computations performed on the Earth's surface, 3 km above the Earth's surface and at a
583 constant height of 250 km. Differences were derived and analyzed for the combinations of the
584 gravitational functional and elevations levels. As expected, larger differences occur mostly

585 over ocean and ice covered areas where the RET concept considerably changes (compresses)
586 the topographic masses. Interestingly, also considerable differences over continental areas with
587 bedrock above MSL are present most notably for computation points at the height of 250 km.
588 Here the influence of mostly the compression of ocean masses has a considerable impact on
589 continental areas mostly along the global coast lines but also reaching far inland.
590
591 While this study provides a comprehensive look at RET approximation errors for the most
592 commonly used gravitational functionals and evaluation locations earlier studies have focused
593 on specific functionals and/or locations only. Considering all combinations of gravitational
594 functional and elevation levels, the relative importance of differences in relation to the signal
595 – as measured by the percentage of the range in differences in relation to the range in signal –
596 is increasing with ascending order of derivative and decreasing with elevation. As such, the
597 best relative agreement is obtained for the gravitational potential at an elevation of 250 km with
598 a percentage value of 0.06% while the largest relative errors are obtained for the second-order
599 derivatives evaluated 1 m above the Earth's surface where the range in differences are at the
600 same level as the range in signal with a maximum percentage value of 109.97%. In the latter
601 case the second-order derivatives of the gravitational potential derived from the Earth2014 and
602 RET2014 masses have little in common when evaluated over the oceans or ice covered areas.
603 In this case it is paramount to use the more rigorous approach of properly accounting for all
604 topographic masses rather than compressing them to RET masses.
605
606 When considering the required accuracy level of gravitational functional or obtainable level of
607 accuracy of observations, in all cases maximum differences are well beyond reasonable levels,
608 thus the replacement of topographic masses by RET masses would not be suitable. For the
609 gravitational potential maximum differences range between -3.981 m^2s^{-2} and 9.512 m^2s^{-2} when
610 evaluated on the Earth's surface, between -3.758 m^2s^{-2} and 8.356 m^2s^{-2} when evaluated 3 km
611 above the Earth's surface and between -4.610 m^2s^{-2} and 3.818 m^2s^{-2} at an elevation of 250 km.
612 These differences translate into geoid height changes in the range of 0.3 m up to almost 1 m.
613 These maximum modelling errors are unacceptably large when considering a common geoid
614 height accuracy at the cm-level or better.
615
616 In case of the first-order derivatives maximum differences in the three gravity components
617 range between about -20 mGal and almost 60 mGal. Considering a common observation
618 accuracy of relative gravimeters of about ±0.01 mGal to ±0.1 mGal, this level of maximum

differences would not be acceptable. This also holds for a targeted accuracy of about 1 mGal for marine gravimetry observations (Motao 1995), e.g., maximum differences are present over the oceans. Similarly large maximum differences are present when evaluating at an elevation of 3 km above the Earth's surface. Again this level is too large when considering a targeted accuracy of about 1 mGal of airborne gravimetry observations. When evaluating at an elevation of 250 km the maximum differences in the first-order derivatives are at the level of almost 0.5 mGal.

Finally, for the second derivatives, maximum differences close to the Earth's surface are at the level of several hundred Eötvös, which is at the same level as the signal and totally unacceptable when considering an achievable accuracy of about 1 E, e.g. using a torsion balance (Völgyesi 2001). As such, the use of the RET approximation renders a topographic potential model useless for smoothing or reducing observations of gravity or vertical deflection gradients.

When evaluating at an elevation of 3 km above the Earth's surface maximum differences decrease to a level of several 10 E (up to a maximum of almost 70 E). While maximum differences considerably drop to a level of about 20 mE (up to a maximum of 52 mE) when evaluating at a height of 250 km. However, they are still considered too large when compared to a GOCE observation accuracy of about 1-2 mE (Rummel et. al 2011) as has been shown by Grombein at al. (2010).

While the RET concept might be suitable when dealing with distant masses only, e.g. small differences over continental areas, due care must be exercised when modelling in coastal areas and areas extending several hundred kilometers inland. Even though over these areas topographic and RET masses are identical, the compression of ocean and ice masses can have considerable impact. A more detailed study is required in these areas to see the full impact, which is beyond the scope of this study. Further, a more detailed study is required when using RET masses only to model more distant masses (e.g. Makhloof and Ilk 2008b) while using the rigorous approach for masses in the vicinity of the computation point. In this case it can be expected that maximum differences are much smaller than that present in this study.

As a central conclusion of our study, the RET approximation in topographic gravity modelling cannot be considered acceptable for most of the first- and second-order derivatives of the

gravity functionals at all elevation levels considered. Therefore, the rigorous calculation of the gravitational potential and its first- and second-order derivatives by properly considering all individual mass components – without compression – should be used. This finding holds for gravity field modelling both in the spatial domain (Kuhn et al. 2009) and the spectral domain (e.g., Hirt and Kuhn 2012, 2014; Claessens and Hirt 2013, Tenzer et al. 2016).

Considering the ever-increasing computational resources, combined with the availability of parallel computing, the additional computational burden for the rigorous calculation even at global scale with high resolution is becoming less of a constraint. This has been successfully demonstrated by this study, based on many calculation runs at a global 5 arc-minute resolution requiring a total of about 50,000 CPU hours (approx. 5.7 years). We acknowledge that the computation time can considerably vary depending on the computation platform and degree of optimization used.

Acknowledgements

We thank for access to the Pawsey Supercomputing Centre (www.pawsey.org.au) through the merit allocation scheme used for the calculations presented in this work. Christian Hirt thanks the German National Research Foundation for support via grant Hi 1760. We are grateful to Prof Mehdi Eshagh and two anonymous reviewers for their thorough reviews and attention to detail.

Appendix A

In order to analytically prove that the RET concept formulated in section 2.2 holds for both masses above and below MSL we first show the derivation for ocean water masses located exclusively below MSL and then for ice masses that can be located partly above and partly below MSL (cf. Figure A1). With respect to an upper crust with the mean density ρ_0, the ocean water masses are considered as mass deficiencies with the density difference $\Delta\rho_{OCN} = \rho_0 - \rho_{OCN}$ where ρ_{OCN} is the density of ocean water. In this case mass equivalence between anomalous ocean water masses and compressed RET masses is expressed by the condition (cf. Eq. 3)

$$\rho_0 \left[R_{up}^3 - \left(R_{low} + \Delta H_c \right)^3 \right] = \Delta\rho_{OCN} \left[R_{up}^3 - R_{low}^3 \right] \qquad \text{(A1)}$$

which can be re-arranged to

$$\rho_0 \left[\left(R_{low} + \Delta H_c \right)^3 - R_{low}^3 \right] = \rho_{OCN} \left[R_{up}^3 - R_{low}^3 \right] \qquad \text{(A2)}$$

by introducing $\Delta\rho_{OCN} = \rho_0 - \rho_{OCN}$. Solving Eq. A2 for ΔH_c, measured above the bedrock, results into

$$\Delta H_c = \sqrt[3]{\frac{\rho_{OCN}}{\rho_0}\left(R_{up}^3 - R_{low}^3\right) + R_{low}^3} - R_{low}, \quad \text{(A3)}$$

which is identical to the general formula derived in section 2.2 for the general RET concept (cf. Eq. 4).

When considering ice masses, in general, we are dealing with anomalous masses above and below MSL with the respective mass densities ρ_{ICE} and $\Delta\rho_{ICE} = \rho_0 - \rho_{ICE}$ (cf. Figure A1). As mass anomalies above and below MSL represent mass excess (positive) and deficiency (negative), respectively, the height H_{RET} describing the RET masses (cf. Figure A1) is obtained by the mass equivalence between the difference in anomalous ice masses above and below MSL and compressed RET masses expressed by the condition

$$\rho_0\left[\left(R + H_{RET}\right)^3 - R^3\right] = \rho_{ICE}\left[R_{up}^3 - R^3\right] - \Delta\rho_{ICE}\left[R^3 - R_{low}^3\right] \quad \text{(A4)}$$

which can be re-arranged to

$$\rho_0\left[\left(R + H_{RET}\right)^3 - R_{low}^3\right] = \rho_{ICE}\left[R_{up}^3 - R_{low}^3\right] \quad \text{(A5)}$$

by introducing $\Delta\rho_{ICE} = \rho_0 - \rho_{ICE}$. Solving Eq. A5 for H_{RET}, measured above/below MSL, results into

$$H_{RET} = \sqrt[3]{\frac{\rho_{ICE}}{\rho_0}\left(R_{up}^3 - R_{low}^3\right) + R_{low}^3} - R. \quad \text{(A6)}$$

Based on H_{RET} the height of all compressed masses (above and below MSL) ΔH_c, measured above the bedrock is obtained by

$$\Delta H_c = H_{RET} - H_{low} = \sqrt[3]{\frac{\rho_{ICE}}{\rho_0}\left(R_{up}^3 - R_{low}^3\right) + R_{low}^3} - R_{low}, \quad \text{(A7)}$$

which again is identical to the general formula given by Eq. (4). Similarly, the RET height can be obtained for lake water masses, which also can be located above and below MSL.

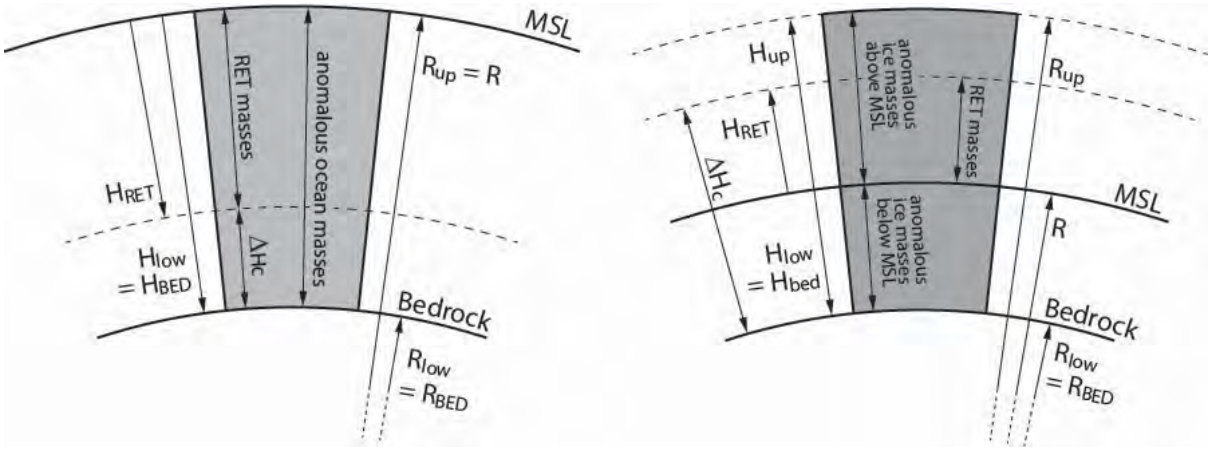

Figure A1: RET principle in spherical approximation for ocean water masses (left) and ice masses (right).

References

Anderson EG (1976) The effect of topography on solutions of Stokes' problem. Unisurv S-14 Report, *School of Surveying*, University of New South Wales, Kensington.

Arkani-Hamed J (1970) Lateral variations of density in the mantel. *Geophysical Journal of the Royal Astronomical Society* 20:431-455.

Audet P (2014) Toward mapping the effective elastic thickness of planetary lithospheres from a spherical wavelet analysis of gravity and topography. *Physics of the Earth and Planetary Interiors* 226:48-82.

Bagherbandi M (2011) An isostatic Earth crustal model and its applications. PhD thesis, Royal Institute of Technology (KTH) Division of Geodesy and Geoinformatics, 224 pp.

Balmino G, Lambeck K, Kaula WM (1973) A spherical harmonic analysis of the Earth's Topography. Journal of Geophysical Research 78(2):478-481.

Balmino G, Vales N, Bonvalot S, Briais A (2012) Spherical harmonic modelling to ultra-high degree of Bouguer and isostatic anomalies. Journal of Geodesy 86(7):499-520.

Baran I, Kuhn M, Claessens SJ, Featherstone WE, Holmes S, Vaníček P (2006) A synthetic Earth gravity model designed specifically for testing reginal gravimetric geoid determination algorithms. *Journal of Geodesy* 80:1-16.

Blakeley RJ (1996) Potential Theory in Gravity and Magnetic Applications. Cambridge: Cambridge University Press.

Čadek O, Matyska C (1990) Three-dimensional modelling convection in the Earth's mantle: Influence of the core mantle boundary. Studia Geophysica et Geodaetica 34:278-283.

Čadek O, Matyska C (1991) Mass heterogeneities and convection in the Earth's mantle inferred from gravity and core-mantle boundary irregularities. *Pure and Applied Geophysics* 135(1):107-123.

Chambat F, Valette FG (2005). Earth gravity up to second order in topography and density. *Physics of the Earth and Planetary Interiors* 151:89-106.

Claessens, SJ (2003) A Synthetic Earth Model: Analysis, Implementation, Validation and Application. DUP Science, Delft, The Netherlands.

Claessens SJ, Hirt C (2013) Ellipsoidal topographic potential: New solutions for spectral forward gravity modeling of topography with respect to a reference ellipsoid. *Journal of Geophysical Research* 118(2):5991-6002.

Deng, X.-L., Grombein, T., Shen, W.-B., Heck, B., Seitz, K. (2016) Corrections to "A comparison of the tesseroid, prism and point-mass approaches for mass reductions in gravity field modelling" (Heck and Seitz, 2007) and "Optimized formulas for the gravitational field of a tesseroid" (Grombein et al., 2013) J Geodesy 90(6):585-587

Douch K, Panet I, Pajot-Métivier G, Christophe B, Foulon B, Lequentrec-Lalancette, M-F, Diament M (2015) Error analysis of a new planar electrostatic gravity gradiometer for airborne surveys. *Journal of Geodesy* 89(12):1217-1231.

Eshagh, M. (2009a) Comparison of two approaches for considering laterally varying density in topographic effect on satellite gravity gradiometric data. *Acta Geophysica*, 58(4): 661-686.

Eshagh, M. (2009b) Contribution of 1^{st} – 3^{rd} order terms of a binomial expansion of topographic heights in topographic and atmospheric effects on satellite gravity gradiometric data. *Artificial Satellites*, 44(1): 21-31.

Fellner JJ, Kuhn M, Featherstone WE (2012) Development of a Synthetic Earth Gravity Model by 3D mass optimisation based on forward modelling. *Earth Planets Space* 64:5-12.

Forsberg R (1984) A study of terrain reductions, density anomalies and geophysical inversion methods in gravity field modelling. *Report* 355, Department of Geodetic Science and Surveying, Ohio State University, Columbus.

Forsberg R, Jensen T (2015) New geoid of Greenland: A case study of terrain and ice effects, GOCE and use of local sea level data. International Association of Geodesy Symposia, doi: 10.1007/1345_2015_50.

Göttl F, Rummel R (2009), Geodetic view on isostatic models. *Pure and Applied Geophysics* 166:1247-1260.

Grombein T, Seitz K, Heck B (2010) Modelling topographic effects in GOCE gravity gradients. GEOTECHNOLOGIEN Science Report, vol. 17, 84–93.

Grombein, T., Seitz, K., Heck, B. (2013), Optimized formulas for the gravitational field of a tesseroid. Journal of Geodesy, 87:645-660.

Grombein T, Seitz K, Heck B (2014a) Topographic-isostatic reduction of GOCE gravity gradients. In: Rizos C, Willis P (eds), Earth on the edge: science for a sustainable planet, Proceedings of the IAG General Assembly, Melbourne, Australia, 2011, IAG Symposia, vol. 139, Springer, 349–356.

Grombein T, Luo X, Seitz K, Heck B (2014b) A wavelet-based assessment of topographic-isostatic reductions for GOCE gravity gradients. *Surveys in Geophysics* 25:959-982.

Grüninger W (1990) Zur topographisch-isostatischen Reduktion der Schwere. *PhD Thesis*, Universität Karlsruhe.

Haagmans R (2000) A synthetic Earth for use in geodesy. *Journal of Geodesy* 74:503-511.

Heck B, Wild F (2005) Topographic-isostatic reductions in satellite gravity gradiometry based on a generalized condensation model. In: Sansò, F (ed) A window on the future of geodesy, IAG Symposia 128, Springer, Berlin pp 294–299.

Heck B, Seitz K (2007) A comparison of the tesseroid, prism and point-mass approaches for mass reductions in gravity field modelling. *Journal of Geodesy*, 81(2):121-136.

776 Hirt C, Kuhn M (2012) Evaluation of high-degree series expansions of the topographic potential to higher-order
777 powers. *Journal of Geophysical Research* 117:B12407.
778 Hirt C (2013) RTM gravity forward-modeling using topography/bathymetry data to improve high-degree global
779 geopotential models in the coastal zone. *Marine Geodesy*, 36(2):1-20.
780 Hirt C, Claessens SJ, Fecher T, Kuhn M, Pail R, Rexer M (2013) New ultrahigh-resolution picture of the Earth's
781 gravity field. *Geophysical Research Letters* 40:4279-4283.
782 Hirt C (2014) GOCE's view below the ice of Antarctica: Satellite gravimetry confirms improvements in Bedmap2
783 bedrock knowledge. *Geophysical Research Letters* 41:5021-5028.
784 Hirt C, Kuhn M (2014) Band-limited topographic mass distribution generates full-spectrum gravity field: Gravity
785 forward modeling in the spectral and spatial domains revisited. *Journal of Geophysical Research: Solid*
786 *Earth* 119(4):3646-3661.
787 Hirt C, Kuhn M, Claessens SJ, Pail R, Seitz K, Gruber T (2014) Study of the Earth's short-scale gravity field
788 using the ERTM2160 gravity model. *Computers & Geosciences* 73:71-80.
789 Hirt C, Rexer M (2015) Earth2014: 1 arc-minute shape, topography, bedrock and ice-sheet models – Available as
790 gridded data and degree-10,800 spherical harmonics. *International Journal of Applied Earth Observation*
791 *and Geoinformation* 39:103-112.
792 Hirt C, Rexer M Claessens SJ (2015) Topographic evaluation of fifth-generation GOCE gravity field models –
793 globally and regionally. *Newton Bulletin* 5:163-186.
794 Hirt C, Rexer M, Scheinert M, Pail R, Claessens SJ, Holmes S (2016) A new degree-2190 (10 km resolution)
795 gravity field model for Antarctica developed from GRACE, GOCE and Bedmap2 data. *Journal of Geodesy*
796 90(2):105-127.
797 Hofmann-Wellenhof, B., Moritz, M. (2005) *Physical Geodesy*, Springer, Wien, New York, pp. 403.
798 Jekeli C (1983) A numerical study of the divergence of spherical harmonic series of the gravity and height
799 anomalies at the Earth's surface. *Bulletine Géodésique* 57:10-28.
800 Kalberg T, Gohl K, Eagles E, Spiegel C (2015) Rift processes and crustal structure of the Amundsen Sea
801 Embayment, West Antarctica, from 3D potential field modelling. *Marine Geophysical Research* 36:263-
802 279.
803 Kirby JF, Swain CJ (2008) An accuracy assessment of the fan wavelet coherence method for elastic thickness
804 estimation. *Geochemistry, Geophysics, Geosystems* 9(3):Q03022.
805 Kuhn M (2000) Geoidbestimmung unter Verwendung verschiedener Dichtehypothesen. Reihe C, Heft Nr. 520.
806 *Deutsche Geodätische Kommission*, München.
807 Kuhn M (2003) Geoid determination with density hypotheses from isostatic models and geological information.
808 *Journal of Geododesy* 77(1-2):50-65.
809 Kuhn M, Featherstone WE (2003) On the Construction of a Synthetic Earth Gravity Model. In: *Proceed 3rd*
810 *Meeting of the Intern. Gravity and Geoid Commission*, ed. I Tziavos, 189-194. Editions Ziti.
811 Kuhn M, Featherstone WE (2005a) Construction of a synthetic Earth gravity model by forward gravity modelling.
812 In F. Sanso (ed.): *A Window on the Future of Geodesy*, IAG Symposia vol. 128, 350-355.
813 Kuhn M, Seitz K(2005), Comparison of Newton's Integral in the Space and Frequency Domains. In *A Window on*
814 *the Future of Geodesy*. IAG Symposia vol. 128, ed F Sanso, 386-391.

Kuhn M, Featherstone WE, Kirby JF (2009) Complete spherical Bouguer gravity anomalies over Australia. *Australian Journal of Earth Science* 56:213-223.

Lambeck K (1976) Lateral density anomalies in the upper mantle. *Journal of Geophysical Research*. 81(35):6333-6340.

Lambeck K (1979) Methods and geophysical applications of satellite geodesy. *Rep. Prog. Phys*. 42:547-628.

Lee WHK, Kaula WM (1967) A spherical harmonic analysis of the Earth's Topography. *Journal of Geophysical Research*. 72(2):753-758.

Llubes M, Florsch N, Legresy B, Lemoine JM, Loyer S, Crossley D, Remy F (2003) Crustal thickness in Antarctica from CHAMP gravimetry. *Earth and Planetary Science Letters* 212:103– 117.

Mader K (1951) Das Newtonsche Raumpotential prismatischer Körper und seine Ableitungen bis zur dritten Ordnung. *Sonderheft 11 der Österreichischen Zeitschrift für Vermessungswesen. Österreichischer Verein für Vermessungswesen, Wien.*

Makhloof AAE, Ilk KH (2008a) Effects of topographic-isostatic masses on gravitational functionals at the Earth's surface and at airborne and satellite altitudes. *Journal of Geodesy* 82:93-111.

Makhloof AAE, Ilk KH (2008b) Far-zone effects for different topographic-compensation models on a spherical harmonic expansion of the topography. *Journal of Geodesy* 82:613-635.

Matyska C (1989) The Earth's gravity field and constraints to its density distribution, *Studia Geophysica et Geodaetica* 33:1-10.

McKenzie D (2010) The influence of dynamically supported topography on estimates of Te. *Earth and Planetary Science Letters* 295:127-138.

McKenzie D, Yi W, Rummel R (2015) Estimates of Te for continental regions using GOCE gravity. *Earth and Planetary Science Letters* 428:97-107.

Moritz H, Hofmann-Wellenhof B (1993) Geometry, Relativity, Geodesy, Wichman, Karlsruhe, 367 pp.

Motao H (1995) Marine gravity surveying line system adjustment. *Journal of Geodesy* 70:158-165.

Nagy D (1966) The gravitational attraction of a right rectangular prism. *Geophysics* 31:362-371.

Nagy D, Papp G, Benedek J (2000) The gravitational potential and its derivatives for the prism. *Journal of Geodesy* 74(7):552-560, Erratum in *Journal of Geodesy*,76(8):475.

Pavlis NK, Rapp RH (1990) The development of an isostatic gravitational model to degree 360 and its use in global gravity modelling. *Geophysical Journal International* 100:369-378.

Petrov O, Morozov A, Shokalsky S, Kashubin S, Artemieva IM, Sobolev N, Petrov E, Ernst, RE, Sergeev S, Smelror M (2016) Crustal structure and tectonic model of the Arctic region. *Earth Science Reviews* 154:29-71.

Rapp RH (1982) Degree variances of the Earth's potential, topography and its isostatic compensation. *Bulletine Géodésique* 56(2):84-94.

Rapp RH (1989) The decay of the spectrum of the gravitational potential and the topography for the Earth. *Geophysical Journal International* 99:449-455.

Rexer M, Hirt C (2015) Spectral analysis of the Earth's topographic potential via 2D-DFT: a new data-based degree variance model to degree 90,000. *Journal of Geodesy*, 89:887-909.

853 Rummel R, Rapp RH, Sünkel H, Tscherning CC (1988) Comparisons of global topographic/isostatic models to
854 the Earth's observed gravity field. *Report* No 388, Dep. Geodetic Sci. Surv., Ohio State University,
855 Columbus, Ohio.
856 Rummel R, Yi W, Stumer C (2011) GOCE gravitational gradiometry. *Journal of Geodesy* 85(11):777-790.
857 Sleep NH, Fujita K (1997) *Principles of geophysics*. Blackwell Sciences, Massachusetts, 586 pp.
858 Stark CP, Stewart J, Ebinger CJ (2003) Wavelet transform mapping of effective elastic thickness and plate
859 loading: Validation using synthetic data and application to the study of southern African tectonics. *Journal*
860 *of Geophysical Research* 108(B12):2558.
861 Sünkel H (1985) *An isostatic Earth model*. Report No 368, Dep. Geodetic Sci. Surv., Ohio State University,
862 Columbus, Ohio.
863 Tenzer R, Abdalla A,Vajda P, Hamayun (2010) The spherical harmonic representation of the gravitational field
864 quantities generated by the ice density contrast. *Contrib. Geophys. Geod.* 40(3):207–223.
865 Tenzer R, Hirt C, Novák P, Pitonák M, Šprlák M (2016) Contribution of mass density heterogeneities to the
866 quasigeoid-to-geoid separation. *Journal of Geodesy* 90(1):65-80.
867 Tsoulis D (1999) Spherical harmonic computations with topographic/isostatic coefficients. IAPG/FESG Report
868 No. 3, Institut fur Astronomische und Physikalische Geodäsie, Universität München, Germany.
869 Tsoulis D (2001) Terrain correction computations for a densely sampled DTM in the Bavarian Alps. *Journal of*
870 *Geodesy* 75:291-307.
871 Tsoulis D, Kuhn M (2007) Recent developments in synthetic Earth gravity models in view of the availability of
872 digital terrain and crustal databases of global coverage and increased resolution. In A. Kiliçoğlu and R.
873 Forsberg (eds.), Gravity Field of the Earth, Proceedings of the 1st International Symposium of the
874 International Gravity Field Service, 354-359, Harita Dergisi, Istanbul, Turkey.
875 Tsoulis D, Patlakis K (2013) A spectral review of current satellite-only and combined Earth gravity models.
876 *Reviews of Geophysics* 51:186-243.
877 Tziavos IN, Sideris MG (2013) Topographic Reductions in Gravity and Geoid Modeling. In: F. Sansò and M.G.
878 Sideris (eds.), *Geoid Determination*, Lecture Notes in Earth System Sciences 110, Springer-Verlag Berlin
879 Heidelberg.
880 Wild F, Heck B (2005) A comparison of different isostatic models applied to satellite gravity gradiometry. In
881 Jekeli, C., Bastos, L., Fernandes, J. (eds) Gravity, geoid and space missions, IAG Symposia 129, Springer,
882 Berlin, pp 230–235.
883 Wild-Pfeiffer, F. (2008) A comparison of different mass elements for use in gravity gradiometry. Journal of
884 Geodesy 82: 637–653.
885 van Hees GLS (2000) Some elementary relations between mass distributions inside the Earth and the geoid and
886 gravity field. *Journal of Geodynamics* 29:111-123.
887 Völgyesi L (2001) Geodetic application of torsion balance measurements in Hungary. Reports on Geodesy,
888 Warsaw University of Technology, Vol. 57, No. 2, 524-531.
889 Wieczorek MA (2015) Gravity and Topography of the Terrestrial Planets. In: Treatise on Geophysics (second
890 edition), (Ed. G. Schubert), 153–193.
891 Zhang Y (2005) Global tectonic and climatic control of mean elevation of continents, and Phanerozoic sea level
892 change. *Earth and Planetary Science Letters* 237:524-531.